AGU PUBLICATIONS

JGR

Journal of Geophysical Research: Planets

RESEARCH ARTICLE

10.1002/2017JE005341

This article is a companion to Panning et al. (2018), https://doi.org/10.1002/2017JE005332 and Stähler et al. (2018), https://doi.org/10.1002/2017JE005338.

Key Points:
- We examine possible ice thicknesses, mineralogy, and porosity in icy ocean worlds consistent with spacecraft and thermodynamic data
- We identify available and needed thermodynamics of ices, oceans, silicates, and metals
- We examine the influences of ocean composition and depth-dependent ocean density on tidal dissipation

Supporting Information:
- Supporting Information S1

Correspondence to:
S. D. Vance,
svance@jpl.nasa.gov

Citation:
Vance, S. D., Panning, M. P., Stähler, S., Cammarano, F., Bills, B. G., Tobie, G., … Banerdt, B. (2018). Geophysical investigations of habitability in ice-covered ocean worlds. *Journal of Geophysical Research: Planets Planets*, *123*, 180–205. https://doi.org/10.1002/2017JE005341

Received 4 MAY 2017
Accepted 15 OCT 2017
Accepted article online 30 NOV 2017
Published online 25 JAN 2018
Corrected 17 MAY 2018

This article was corrected on 17 MAY 2018. See the end of the full text for details.

Geophysical Investigations of Habitability in Ice-Covered Ocean Worlds

Steven D. Vance[1], Mark P. Panning[1], Simon Stähler[2,3], Fabio Cammarano[4], Bruce G. Bills[1], Gabriel Tobie[5,6], Shunichi Kamata[7], Sharon Kedar[1], Christophe Sotin[1], William T. Pike[8], Ralph Lorenz[9], Hsin-Hua Huang[10,11], Jennifer M. Jackson[10], and Bruce Banerdt[1]

[1] Jet Propulsion Laboratory, California Institute of Technology, Pasadena, CA, USA, [2] Institute of Geophysics, ETH Zürich, Zürich, Switzerland, [3] Leibniz-Institute for Baltic Sea Research (IOW), Rostock, Germany, [4] Laboratoire de Planétologie et Géodynamique, Dipartimento di Scienze Geologiche, Universita Roma Tre, Rome, Italy, [5] Université de Nantes, Nantes, France, [6] CNRS, Nantes, France, [7] Creative Research Institution, Hokkaido University, Sapporo, Japan, [8] Department of Electrical and Electronic Engineering, Imperial College, London, UK, [9] Johns Hopkins University Applied Physics Laboratory, Laurel, MD, USA, [10] Seismological Laboratory, California Institute of Technology, Pasadena, CA, USA, [11] Institute of Earth Sciences, Academia Sinica, Taipei, Taiwan

Abstract Geophysical measurements can reveal the structures and thermal states of icy ocean worlds. The interior density, temperature, sound speed, and electrical conductivity thus characterize their habitability. We explore the variability and correlation of these parameters using 1-D internal structure models. We invoke thermodynamic consistency using available thermodynamics of aqueous $MgSO_4$, NaCl (as seawater), and NH_3; pure water ice phases I, II, III, V, and VI; silicates; and any metallic core that may be present. Model results suggest, for Europa, that combinations of geophysical parameters might be used to distinguish an oxidized ocean dominated by $MgSO_4$ from a more reduced ocean dominated by NaCl. In contrast with Jupiter's icy ocean moons, Titan and Enceladus have low-density rocky interiors, with minimal or no metallic core. The low-density rocky core of Enceladus may comprise hydrated minerals or anhydrous minerals with high porosity. *Cassini* gravity data for Titan indicate a high tidal potential Love number ($k_2 > 0.6$), which requires a dense internal ocean ($\rho_{ocean} > 1,200$ kg m^{-3}) and icy lithosphere thinner than 100 km. In that case, Titan may have little or no high-pressure ice, or a surprisingly deep water-rock interface more than 500 km below the surface, covered only by ice VI. Ganymede's water-rock interface is the deepest among known ocean worlds, at around 800 km. Its ocean may contain multiple phases of high-pressure ice, which will become buoyant if the ocean is sufficiently salty. Callisto's interior structure may be intermediate to those of Titan and Europa, with a water-rock interface 250 km below the surface covered by ice V but not ice VI.

Plain Language Summary Seismometers, magnetometers, and other tools may be used in the future to glimpse the insides of ocean worlds-moons of Jupiter and Saturn that have lots of liquid water under their icy surfaces. These measurements could reveal whether water and rock interact to produce chemical conditions that on Earth support life, how much life such chemical activity might support, and how long that activity has persisted through time. The pressures and temperatures in these extraterrestrial oceans differ from those in Earth's oceans, so only just now are the needed tools and data becoming available to predict what future measurements might reveal. In this work, we investigated the interior structures of icy ocean worlds based on available information—mainly NASA's Galileo and Cassini missions—and used chemical data to test what ocean and rock compositions are possible. Our calculations make predictions for Saturn's moons: Titan should not have an iron core, and its ocean may contain little or no high-pressure ice. Fluids may flow through the whole of the rock core of Enceladus because Cassini gravity measurements seem to point to a porous interior. Geophysical investigations could test whether the ocean in Jupiter's moon Europa has a composition like Earth's or may instead by very acidic if water and rock have not interacted much. Our calculations predict that these two scenarios can create unique combinations of measurable properties that can be probed by future missions using seismology, magnetic field measurements, and other means.

1. Introduction

Geophysical measurements can reveal the interior properties of icy ocean worlds. Such measurements can point to the presence and temporal variability of fluids and gases, thus identifying potential habitable niches for life (Vance et al., 2017). The thickness and geodynamics of different ice phases, and the depth of the ocean, determine the conditions under which life might exist. The global fluxes of chemical energy must be understood in terms of a world's interior structure and evolution (Vance, Hand, et al., 2016). Such a global picture is necessary for quantifying the types of life and amounts of biomass that might be supported (Shock & Holland, 2007). This is also required for interpreting any potential indications of life that might be found through in situ sampling, as, for example, by a lander on Europa's surface (Hand et al., 2017).

In Ganymede, Callisto, and Titan, the predicted presence of high-pressure ices has been regarded as a barrier to water-rock interactions. However, this seems like less of an impediment now, in light of recent studies of fluids within and under the ices. Convection within the ices should proceed near the solidus temperature, leading to melt at the high-pressure ice and rock interface, and within the upper parts of the high-pressure ice (Choblet et al., 2017; Kalousová et al., 2018). Briny fluids under pressure can have densities exceeding those of high-pressure ices and thus may occupy the interface between rock and ice (Hogenboom, 1995; Journaux et al., 2013; Vance et al., 2014) or between the different layers of high-pressure ice (Journaux et al., 2017; Vance & Brown, 2013). Dissolved ions can incorporate into high-pressure ice VI (and possibly also in ice phases II, III, and V) to a much greater extent than in ice Ih, potentially decreasing the density of the ices and enhancing near-solidus convection (Journaux et al., 2017).

The combination of seismology with other methods may be deployed at other ocean worlds to reveal the nature of potential habitats in the ice, ocean, seafloor, and regions below. Seismic investigations could constrain the habitability of ocean worlds (Vance et al., 2017) in a manner that is complementary to other measurements by missions exploring the habitability of ocean worlds. NASA's planned Europa Clipper mission (Pappalardo et al., 2016) and ESA's JUICE mission (Grasset et al., 2013) will use ice-penetrating radar sounding investigations to constrain the density, temperature, and composition of the ices covering Europa, Ganymede, and Callisto. The RIME and REASON instruments will reveal the upper kilometer of the ice with a range resolution as small as 15 m and will sound to as much as 9 and 45 km, respectively, in cold ice with a range resolution as small as 30 m (Bruzzone et al., 2013; Grima et al., 2015). Whereas radio waves are sensitive mainly to density, electrical conductivity, and crystal orientation fabric (COF), seismic waves are influenced mainly by elastic parameters, COF, and temperature (Diez, 2013). Prior radar information thus provides a powerful constraint for extracting more detailed information from the deeper interior. Similar combined investigations of Antarctic glaciers have revealed a sub-ice lake and low-velocity layers at the water-rock interface consistent with a sedimentary layer (Bell et al., 1998). Additional prior information will be obtained by magnetic field and charged particle measurements (ICEMAG and PIMS) on the planned Europa Clipper, using Europa's induced response to Jupiter's time-varying magnetic field to constrain the ocean's depth and electrical conductivity. The internal structure and tidal dissipation will be investigated from radio tracking measurements of gravity to high order and degree and geodetic and librational measurements from imaging and altimetry (Mazarico et al., 2015; Park et al., 2015; Van Hoolst et al., 2013). As a follow-on, seismology could directly measure the ice and ocean thicknesses and could leverage constraints on electrical conductivity and internal structure to narrow the range of plausible models for ocean salinity. Seismic measurements might also probe below the ocean to reveal the deeper structure, with the potential to constrain the current thermal state of the rocky interior (Cammarano et al., 2006).

Here we develop global one-dimensional models to assess how combined seismic, gravity, and magnetic measurements may be used to investigate the habitability of ocean worlds. We use the models to consider how the ocean's composition might couple to the configurations and thicknesses of ice layers. We also use the models to test the limits of available data describing material properties. In section 2, we describe the workings of the model and limitations of available data. In section 3, we describe applications to confirmed ocean worlds, Ganymede, Europa, Enceladus, Titan, and Callisto. In sections 4 and 5 we discuss possible tests for habitability and thermodynamic measurements needed for further modeling.

2. Materials and Methods

We model the interior density, elastic, and anelastic structure and associated seismic sources and signatures in icy ocean worlds, building on prior work that focused only on Europa (Cammarano et al., 2006). Added to this is an investigation of the electrical conductivity of fluids based on available measurements.

Table 1
Properties of Known Icy Ocean Worlds

	Radius (km)	Density (kg m^{-3})	Moment of inertia
Europa[a]	$1,561.0 \pm 8.0$	$2,989 \pm 46$	0.346 ± 0.005
Ganymede[b]	$2,631 \pm 1.7$	$1,942.0 \pm 4.8$	0.3115 ± 0.0028
Callisto[c]	$2,410.3 \pm 1.5$	$1,834.4 \pm 3.4$	0.3549 ± 0.0042
Enceladus[d]	$2,52.1 \pm 0.2$	$1,609 \pm 5$	0.335
Titan[e]	$2,574.73 \pm 0.09$	$1,879.8 \pm 0.004$	0.3438 ± 0.0005

[a]Anderson (1998), Wahr et al. (2009). [b]Schubert et al. (2004), revised from Anderson et al. (1996). [c]Anderson (2001). [d]Thomas (2010) and less et al. (2014). [e]Jacobson et al. (2006) and less et al. (2012).

The interior structure model used in the present work builds on the one described in Vance et al. (2014). It propagates density and temperature profiles downward from the ice Ih layer, based on boundary conditions of the surface temperature (T_s) and temperature at the ice-ocean interface (T_b). The pressure-temperature profiles in the H_2O-rich uppermost layer (see supporting information S2 and S3) are propagated through the ocean, assuming uniform salinity and adiabatic convection. The depths of the transitions between compositional layers (ice, ocean, (ice), rock, and (iron-rich core)) are then computed from bulk density and gravitational moment of inertia (C/MR^2; Table 1). We note that independent measurements of C_{22} and J_2 were not obtained for the Galilean satellites, and so prior analyses have assumed that they are in hydrostatic equilibrium. This assumption may lead to an overestimation of up to 10% for the moment of inertia of the slowly rotating moon, Callisto (Gao & Stevenson, 2013). We consider this effect in section 3. The model now accounts for solid-state convection in the ice Ih layer, by iteration after the initial model run (see supporting information) based on the inferred ice thickness. As in Vance et al. (2014), temperature profiles in the high-pressure ices follow the melting curves, in basic approximation of two-phase convection. Because gravitational acceleration increases with depth in the low-density ice and liquid layers (by up to 25% in the case of Ganymede; Vance et al., 2014), depth-dependent gravity is computed in the H_2O-rich upper layer. Gravity is evaluated at the top of the rock and iron-rich core layers and held constant within them.

2.1. Material Properties

2.1.1. Ices

The thermodynamic properties of water ice phases Ih, II, III, V, and VI are taken primarily from Choukroun and Grasset (2010), which fit available measurements of heat capacity, enthalpy, and specific volume over the broad range of pressure and temperature occurring in icy worlds. Sound speeds are modified from Shaw (1986) and Gagnon et al. (1988, 1990) as described below. Analysis of the available data, also described below, suggests that further measurements of sound speeds in ices are needed to address thermodynamic inconsistencies.

Compressional and transverse sound speeds in the relevant ice phases are matched to sound speeds from bulk adiabatic Brillouin and ultrasonic measurements in polycrystalline ice at −25 and −35.5°C to 1 GPa (Gagnon et al., 1988, 1990; Shaw, 1986) to within their assigned errors. Adiabatic shear and bulk moduli (G_S, K_S)

Table 2
Bulk and Shear Moduli of Ices

Crystalline phase	K_S[a] GPa	K_S'[b]	K_S'' GPa^{-1}	G_S GPa	G_S'[b]	G_S'' GPa^{-1}
I_h[c]	9.5	0.33	−0.026	3.3	0.537	−0.025
II	13.89	1.6	—	5.15	3.5	—
III	8.9	3.65	—	2.7	6.55	—
V	11.8	4.8	—	5.7	0.9	—
VI	14.6	4.1	—	5.0	3.0	—

[a]Adapted from Gagnon et al. (1990). [b]Fit from Shaw (1986). [c]Gagnon et al. (1988).

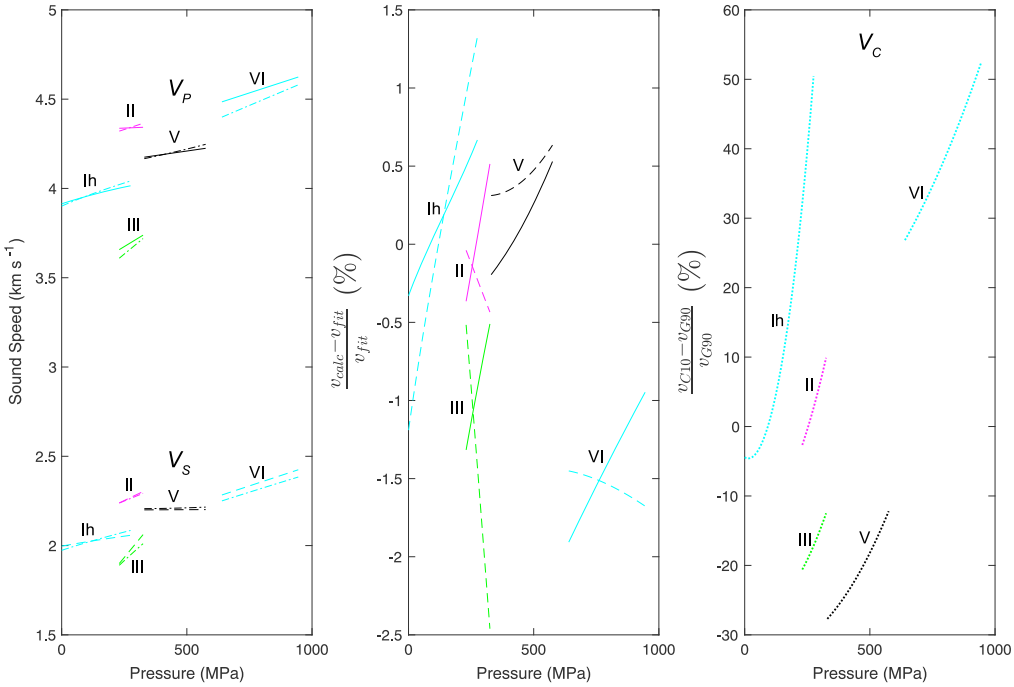

Figure 1. Comparison of sound speeds at ~240 K (−35.5°C) with polynomial fits to measurements from Gagnon et al. (1990, G90). (left) Sound speeds (V_P, lines, and V_S; dashed lines from G90; dash-dotted lines from this work) for ices Ih, II, III, V, and VI. (middle) Deviations (%) between published and fit values (V_P, lines, and V_S; dashed lines). (right) (dotted line) Deviations (in %) of bulk sound speeds (equation (3)) from those of the ice thermodynamics adopted for this work (Choukroun & Grasset, 2010, C10).

and their pressure derivatives (Table 2) are adjusted from Shaw (1986) to fit compiled sound speeds from Gagnon et al. (1990) to better than 1.5% (Figure 1). Sound speeds (Figure 2) are computed as

$$V_S = \left[\frac{G_S}{\rho}\right]^{1/2}, \tag{1}$$

$$V_P = \left[\frac{K_S}{\rho} + \frac{4}{3}V_S^2\right]^{1/2}. \tag{2}$$

This strategy does not reproduce the reported negative slopes of sound speeds with temperature in laboratory ice Ih at 0.1 MPa ($\{\partial V_P/\partial T, \partial V_S/\partial T\} \approx \{-2.81, -1.43\}$ m s^{-1} K^{-1}; Vogt et al., 2008).

To assess the accuracy of the adopted ice thermodynamics relative to available sound speed measurements, we compute the corresponding bulk sound speed, V_C (Masters et al., 2000), from

$$V_C = \sqrt{V_P^2 - \frac{4}{3}V_S^2} = \left(\frac{\partial\rho}{\partial P}\right)^{-1/2}. \tag{3}$$

Analytical values of $\partial\rho/\partial P$ were computed from Choukroun and Grasset (2010) densities as described in the supporting information. The computed values of V_C fail to match the bulk speeds based on values compiled by Gagnon et al. (1990), by up to {50, 10, 20, 30, 50}% for ices {I, II, III, V, VI} (Figure 1, right). The corresponding disagreement in density based on the integration of bulk sound speeds is up to 1% (for ice V), assuming that the lowest-pressure values of density from Choukroun and Grasset (2010) are correct (see supporting information). This is within the stated errors of the data (Choukroun & Grasset, 2010). A more satisfactory data set for the present purposes would provide sound speed measurements with sufficient coverage in pressure and temperature to obtain thermodynamically consistent density, heat capacity, etc.

Thermal properties are taken from Andersson and Inaba (2005). Solid-state convection in ice Ih is parameterized as per Deschamps and Sotin (2001). Creep properties are from Durham et al. (1997). Further details are provided in supporting information S3 and S5.

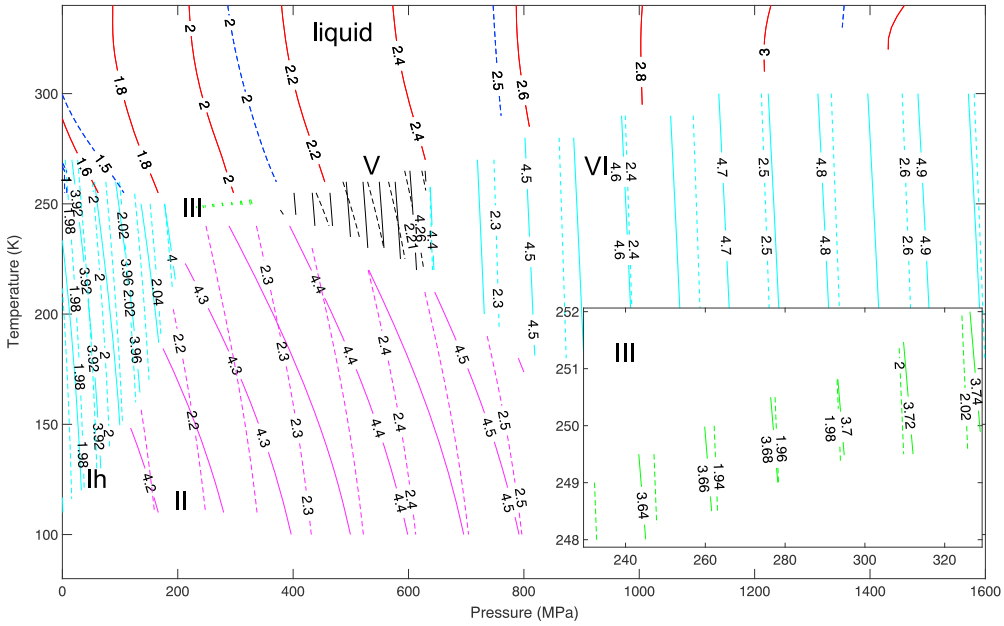

Figure 2. Contours of sound speed versus pressure (MPa) and temperature (K). In the ice stability field ($T \sim< 260$ K): v_P (lines) and v_S (dashed lines), ice Ih, and VI are cyan, ice II is magenta; ice III is green (also shown in the inset); and ice V is black. In the fluid stability range: v_P in 10 wt % $MgSO_4$ (red lines) and pure water (blue dashed lines). Fluid-liquid phase boundaries are for the 10 wt % $MgSO_4$ solution.

2.1.2. Fluids

We examine the influence of salinity in each ocean world by comparing the compositions of pure water and 10 wt % (~1 *m*) $MgSO_4$. Seawater compositions are examined as well for Europa and Enceladus. Solutions containing 3 wt % NH_3 are considered for Titan and Enceladus. The thermodynamic properties used for propagating the adiabatic profiles are density (ρ), thermal expansivity (α), and heat capacity (C_P). Sound speed (v) and electrical conductivity (k_S) are determined using the resulting *P-T* values.

The thermodynamic properties for aqueous magnesium sulfate are from Vance and Brown (2013). The equation of state based on three-dimensional spline interpolation provides the most accurate representation of the data, with smooth extrapolation between 0.8 and 1.6 GPa. The melting point depression is computed using the Margules parameterization for the activity of water for $MgSO_4$ (Vance et al., 2014) and NH_3 (Choukroun & Grasset, 2010). Contours of sound speed for water and 10 wt % $MgSO_4$ are shown in Figure 2.

The Gibbs Seawater package (GSW; McDougall & Barker, 2011) provides thermodynamics for seawater reliably to 100 MPa, with reasonable stability for standard seawater concentration (saline mass fraction of 35.16504 g/kg seawater, containing {10.78145,19.35271} g (Na,Cl) per kilogram of solution; Millero et al., 2008) to the 210 MPa limitation of its equation of state for ice Ih.

Thermodynamics of aqueous ammonia are from the Helmholtz equation of state of Tillner-Roth and Friend (1998) as provided in the REFPROP software package (Lemmon et al., 2007), with ice phase equilibria from Choukroun and Grasset (2010).

The electrical conductivity of 0.01 mol $kg^{-1}_{H_2O}$ (molal) $MgSO_4$ (aq) is computed along geotherms based on measurements at 298 K and 323 K and pressures up to 784.6 MPa (Larionov & Kryukov, 1984). Extrapolation to 273 K is applied with a scaling factor of 0.525, as per Hand and Chyba (2007), with linear interpolation and extrapolation to 250 K and 1.6 GPa. Figure 3 shows the variation of electrical conductivity with pressure, temperature, and concentration of $MgSO_4$ in the main region down to 273 K. Conductivity depends strongly on salt concentration. Direct measurements of conductivity at elevated pressure are unavailable. Measurements taken at standard pressure show a factor of 40 increase for magnesium sulfate up to 1 *m* (Hand & Chyba, 2007, Figure 1). This linear scaling with salt concentration is used in our calculations. GSW includes electrical conductivity for seawater (McDougall & Barker, 2011).

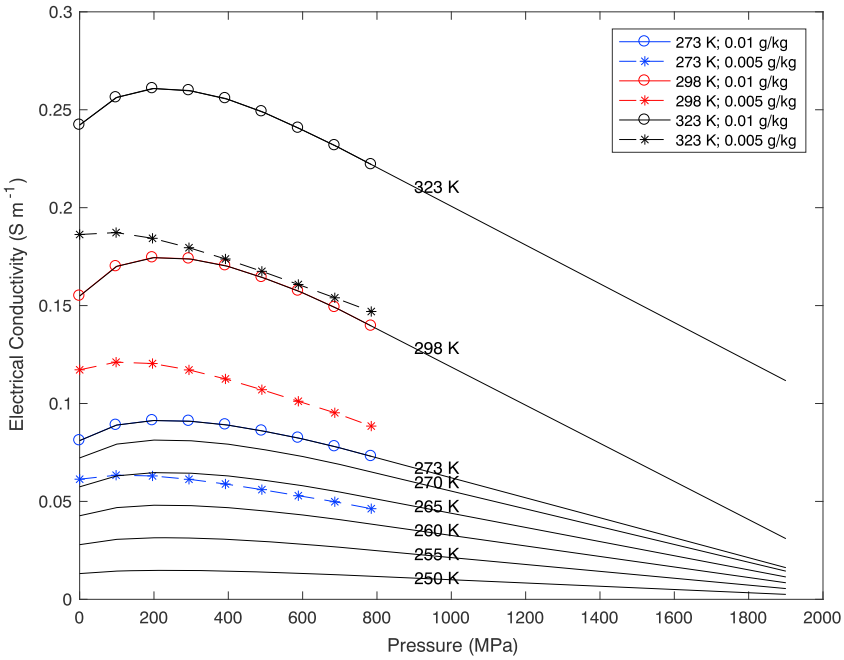

Figure 3. Electrical conductivity of 0.005 *m* and 0.01 *m* $MgSO_4$ from Larionov and Kryukov (1984). Contours show linear extrapolation above 800 MPa and below 273 K for the 0.01 *m* data.

2.1.3. Rock Thermodynamics

We model the silicate interiors of planetary bodies using freely available thermodynamic data and software. Stable mineralogies, densities, and seismic velocities of the bulk rock are determined from the profiles of present-day temperature (*T*), composition (*C*), and pressure (*P*) for representative mineral compositions using PERPLEX 6.7.8 (Connolly, 2005, 2009, http://www.perplex.ethz.ch). The program solves the Gibbs energy minimization based on specified thermodynamic databases and thermoelastic properties for end-member mineralogical phases. Average properties of the bulk rock are determined through a classical Voigt-Reuss-Hill averaging scheme. High-pressure (>5 GPa) polythermal equations of state (Murnaghan, Birch-Murnaghan) were stabilized by specifying the software option to compute the temperature derivative of the bulk modulus as a function of the pressure derivative of the bulk modulus and the expansivity at the reference pressure, as per Helffrich and Connolly (2009).

Following previous work for Europa by Cammarano et al. (2006), we consider two different dry compositions: an Earth-like pyrolite composition and L-LL chondritic model (Table 3). We also consider compositions that include sodium, as per Cammarano et al. (2011). The computations use the formalism and thermoelastic properties data set of Stixrude and Lithgow-Bertelloni (2011), which accounts for six main oxides: SiO_2, MgO, FeO, CaO, Al_2O_3, and Na_2O. The treatment does not include spin transitions. The database was assembled with a focus on using available elastic moduli of Earth's mantle minerals, which extend to pressures in the 100 GPa

Table 3
Chemical Compositions (in Mole Percent) Considered for the Rocky Component

	Pyrolite[a]	L-LL chondrite[b]	Pyrolite[b]	L-LL chondrite[b]
SiO_2	38.71	41.81	38.66	42.78
MgO	49.85	38.73	48.53	39.68
FeO	6.17	14.98	5.72	13.98
CaO	2.94	2.12	3.50	2.13
Al_2O_3	2.22	1.36	3.59	1.43
Na_2O	0.11	1.02	–	–

[a]Cammarano et al. (2011). [b]Modified from Cammarano et al. (2006).

range for select phases. Variations in major oxides, especially in iron content, have the largest effect on density and shear modulus. Densities for both pyrolite and L-LL chondrite composition exceed 3,000 kg m^{-3}. Porosity and hydration must be considered to account for rock densities as low as 2,200 kg m^{-3} allowed by the high values of moment of inertia and low bulk densities for Enceladus. Including these subtleties does not account for densities as low as 2,500 kg m^{-3} for Titan.

The effects of hydrous compositions are considered, using the database of Holland and Powell (2011), which includes more mineral species while retaining thermodynamic self-consistency. We use the same oxide compositions described in the previous section but at partially hydrated or water-saturated conditions. Serpentinization may be important as a source of H_2 for life (e.g., Müntener, 2010; Vance, Hand, et al., 2016), but it may not reduce the density of the rocky siliceous parts of icy worlds because hydrated silicates are not thermodynamically stable at low pressures and at temperatures higher than 900 K (e.g., Ulmer & Trommsdorff, 1995).

For models specifying an iron or iron-rich core, the mean density of the rock is needed as an additional constraint (see supporting information S3). The value of ρ_{rock} is adjusted to match the average predicted by the model ($\rho_{rock,model}$). This is the beginning of a fully iterative approach (Cammarano et al., 2006) that recomputes the gravity and moment of inertia. For the present 1-D models, given the uncertainties in the provided moments of inertia, the current method is deemed sufficient.

2.1.4. Rock Porosity

Because of the low confining pressures occurring in smaller icy ocean worlds, porosity remains important to much greater depths than on Earth. Tidal forcing and thermal fracturing may aid in developing a porous interior, as putatively found at Enceladus (Vance et al., 2007; Waite et al., 2017). In general, porosity decreases with increasing lithostatic pressure, which closes pore spaces, cracks, and fractures. Vitovtova et al. (2014), for example, estimate Earth's mantle porosity at a few percent at a depth of 10 km, decreasing to 0.01–0.1% at 35 km. The trend can be more complex. For example, an *increase* in porosity with depth is recorded for the borehole of the Kola peninsula, the deepest on Earth, at 12 km (Kozlovsky, 1987). We neglect such complexities in this work.

Direct and indirect measurements suggest that the porosity of Earth's oceanic and continental crust is high, especially in the uppermost part (ranging from 5 to 10%; e.g., Carlson 2014). For example, high V_P/V_S at 25–45 km depth suggests a porosity around 2.7–4.0% (Peacock et al., 2011), associated with the presence of fluid saturated zones. Alternatively, crack anisotropy may partially explain the high V_P/V_S (Wang et al., 2012). Experimental studies find that voids close at pressures higher than 0.25 GPa (Kern, 1990) unless fluids fill the voids. Recent laboratory experiments in a porous natural sample of crustal rock (ı.e., Saito et al., 2016) indicate that porosity closure is active up to ~0.6 GPa. In crystalline rocks, the intergranular porosity is usually small but may increase due to water-rock interactions (e.g., Tutolo et al., 2016). Even in areas with low remanent porosity, the effect on seismic velocities can be a few percent and thus should be accounted for. The ratio V_P/V_S, in this case, decreases in the pore spaces not filled by fluids.

Han et al. (2014) estimated the Moon's near-surface porosity to be 10–20% based on *GRAIL* measurements of the Moon's gravity and topography. They interpreted the increase in density with depth to suggest that this porosity is eliminated at 10–20 km depth (200–250 MPa). Pressures at the center of Enceladus do not reach the closure pressure inferred for Earth's Moon. Also, unlike the Moon, icy satellites can have pore spaces filled with fluids, which might allow pores to remain open to pressures exceeding 250 MPa.

We model porosity using the empirical formulation developed by Han et al. (2014). Porosity scales as a function of pressure as

$$\phi(r) = \phi_1 \exp(-cP(r)/P_C), \tag{4}$$

with P the lithostatic confining pressure, ϕ_1 the surface porosity, P_C the closure pressure, and c a constant assumed to be 6.15.

The reduction in density due to porosity is obtained from $\rho = \phi\rho_f + (1-\phi)\rho_g$, where the rock density ρ_g is density obtained from thermodynamic modeling. The pore spaces are assumed to be filled by water; for simplicity, we set $\rho_f = 1,023$ kg m^{-3}.

Seismic velocities are generally expected to decrease with increasing pore pressure. The precise influence of porosity on seismic velocities is complicated by the shape, distribution, and connectivity of pores and the

Table 4
Iron and Iron-Sulfur Properties

	fcc iron[a]	Fe-FeS (melt for 5%< X_{FeS} < 20%)[b]
ρ	8,000	$5,150 - (\%S - 10) \times 50$
α, 10^{-5} K^{-1}	5	9.2
K_S, GPa	156	$53.2 - (\%S - 10) \times 2$
$\partial K_S/\partial P$	5.0	4.66
$\partial K_S/\partial T$, Pa K^{-1}	−0.040	NA
G, GPA	76.5	NA
$\partial G/\partial P$	2	NA
$\partial G/\partial T$, Pa K^{-1}	−0.023	NA

[a]Isaak and Masuda (1995), Klotz and Braden (2000), Voronov and Chernysheva (1999), and Cammarano et al. (2006). [b]Sanloup et al. (2000).

presence of cracks and fractures, and few experiments exist that infer this relation (e.g., Christensen, 1989; Darot & Reuschlé, 2000; Todd & Simmons, 1972; Yu et al., 2016). We parameterize the decrease in V_P as a function of porosity using the relation suggested by Wyllie et al. (1958):

$$\frac{1}{V_{P\phi}} = \frac{\phi}{V_{\text{fluid}}} + \frac{1-\phi}{V_P}. \tag{5}$$

The decrease in V_S should be greater; Christensen (1989) found a decrease of 9% and 26% for V_P and V_S, respectively, when increasing pore pressure from atmospheric pressure to 85% in a very porous (3.9%) lherzolite xenolith at 150 MPa of confining pressure. For models where the maximum decrease in V_P is less than 40%, we assume that the percent decrease in V_S is twice that of V_P. Although approximate, these corrections account for the expected qualitative effects of water-filled porous spaces on seismic velocities.

2.1.5. Rock Electrical Conductivity

Electrical conductivities in Earth's mantle vary with temperature and hydration state over the range 10^{-4} to 10^{-1} S m^{-1} (Huang et al., 2005; Karato, 1990; Wang et al., 2006; Yoshino et al., 2009; Zhao & Yoshino, 2016). They may approach 10^2 S m^{-1} in the lower mantle (Xu et al., 2000). In the present work we do not map the specific variations of electrical conductivity in rock for our adopted compositions, but it is worth noting that the range of lower mantle electrical conductivities overlaps with plausible values in extraterrestrial oceans (Hand & Chyba, 2007).

2.1.6. Iron-Rich Core

When including an iron-rich core, we assume that the core consists of face-centered cubic (or γ) Fe, mixed with FeS up to 5 wt %, or molten Fe-FeS, as described by Cammarano et al. (2006) (Table 4). The density of the solid core for $X_{FeS} < 5\%$ is

$$\rho_{\text{core}} = \frac{\rho_{\text{Fe}}\rho_{\text{FeS}}}{X_{\text{FeS}}(\rho_{\text{Fe}} - \rho_{\text{FeS}}) + \rho_{\text{Fe}}} \tag{6}$$

The choice of core composition does not significantly affect the results for the properties of the deep ocean, which are the main focus of this paper. We assume a high value of conductivity for the iron-rich core (10^7 S m^{-1}; Gomi et al., 2013) and do not consider variations in conductivity with core composition.

2.2. Anelasticity (Seismic Attenuation)

Frequency-dependent seismic attenuation is computed as (Cammarano et al., 2006)

$$\frac{Q_S}{\omega^\gamma} = B_a \exp\left(\frac{\gamma H(P)}{RT}\right), H(P) = g_a T_m \tag{7}$$

with $B_a = 0.56$ a normalization factor, ω the seismic frequency, and exponent $\gamma = 0.2$ the frequency dependence of attenuation. H, the activation enthalpy, scales with the melting temperature T_m with the anisotropy coefficient g_a. Chosen values of g_a for ices {I,II,III,V,VI} are {22, 30 25, 27, 28, 30}. For the rocky mantle we assume $g_a = 30$. If a metallic core is present, the metal's Q_S/ω^γ is set to 10^4.

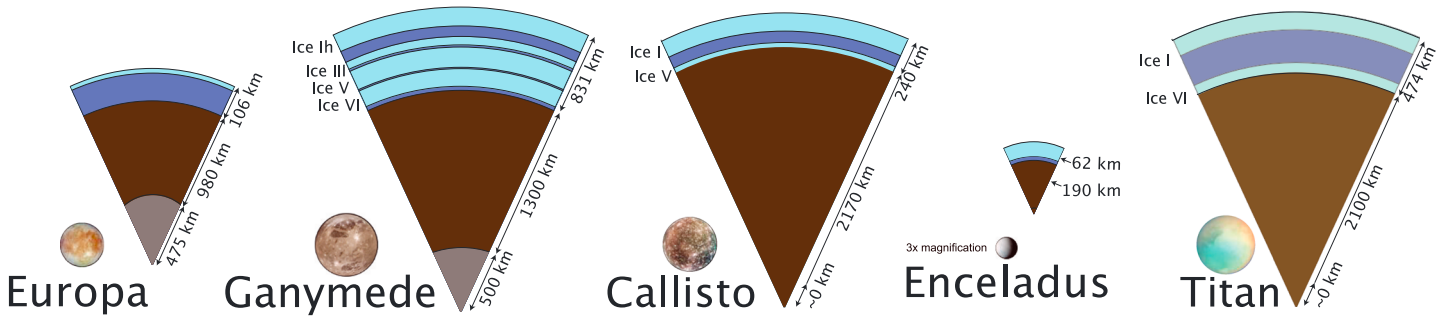

Figure 4. Comparative interior structures of known icy ocean worlds.

2.3. Tidal Deformation

Interior structure determines the response to tidal forcing. The tidal Love number k_2 describes the gravitational potential perturbation at the surface, while h_2 describes the amplitude of the radial surface displacement. They can be obtained from gravity field measurements and laser altimetry of the target body, respectively. In this study, we calculate both k_2 and h_2 for different interior structural models to quantify their tidal responses. From the profiles of density, elasticity (shear and bulk modulus), and viscosity structure determined for each moon, we compute the viscoelastic response of the interior to tidal forcing using the numerical methods of Takeuchi et al. (1972), Saito (1974), and Tobie et al. (2005), as further described in supporting information S6. The dissipative part is represented by the imaginary part of the Love number k_2, or by the dissipation function, Q^{-1}, which corresponds to the ratio between the imaginary part and the modulus of k_2.

Table 5
Ganymede: Pyrolite Composition Containing Na_2O

$MgSO_4$	ρ_{rock} (kg m^{-3})		3,520	
10 wt %	$\rho_{rock,model}$ (kg m^{-3})	3,517	3,510	3,506
	T_b (K)	250	260	270
	q_b mW m^{-2}	3	6	22
	q_c mW m^{-2}	15	18	25
	D_{lh} (km)	157	95	26
	D_{ocean} (km)	24	287	493
	D_{III} (km)	56	-	-
	D_V (km)	150	-	-
	D_{VI} (km)	489	528	411
	R_{rock} (km)	1,759	1,725	1,704
	R_{core} (km)	501	602	661
Water	ρ_{rock} (kg m^{-3})		3,530	
	T_b (K)	255	265	273
	q_b mW m^{-2}	4	8	107
	q_c mW m^{-2}	16	20	107
	D_{lh} (km)	134	70	5
	D_{ocean} (km)	119	361	518
	D_V (km)	139	-	-
	D_{VI} (km)	478	427	331
	R_{rock} (km)	1,764	1,776	1,780
	R_{core} (km)	468	437	447

Note. $Q_{rock} = 100$ GW. $X_{FeS} = 20\%$ and $\rho_{core} = 7,203$ kg m^{-3}.

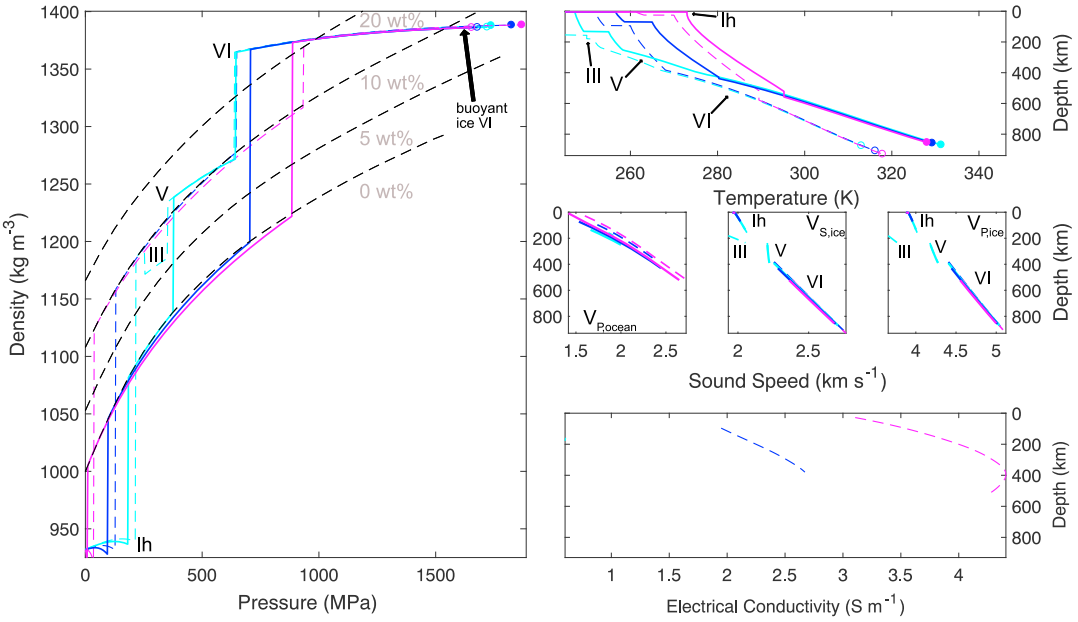

Figure 5. Ganymede: Oceans with 10 wt % $MgSO_4$(aq) (dashed lines) and pure water (lines) for T_b as in Table 5. Magentas are warm profiles with $D_{Ih} < 30$ km, blues are modest temperature profiles with thicker ice Ih, and cyans are colder profiles with $D_{Ih} > 130$ km. (left) Density versus pressure. Reference fluid densities along the melting curve for $MgSO_4$ for {0,5,10,15} wt % increase with increasing salt concentration. (right) Corresponding depth-dependent temperature (top), sound speed in the fluids and ices (fluid, V_S, and V_P, middle left to right), and electrical conductivity (bottom). Circles indicate the transition to the silicate interior.

For comparison, we also apply the methods described in detail in Kamata et al. (2015), adopting the rheology of pure water ice by Goldsby and Kohlstedt (2001) to calculate the viscosity from temperature. Other solid layers are assumed to be elastic; an infinite viscosity is assumed. Although high-pressure ices may have low viscosities, their tidal response is nearly independent of the viscosity of high-pressure ices if an ocean is sandwiched (Kamata et al., 2016). Consequently, this simplification does not affect our conclusions. Liquid layers are assumed to be inviscid.

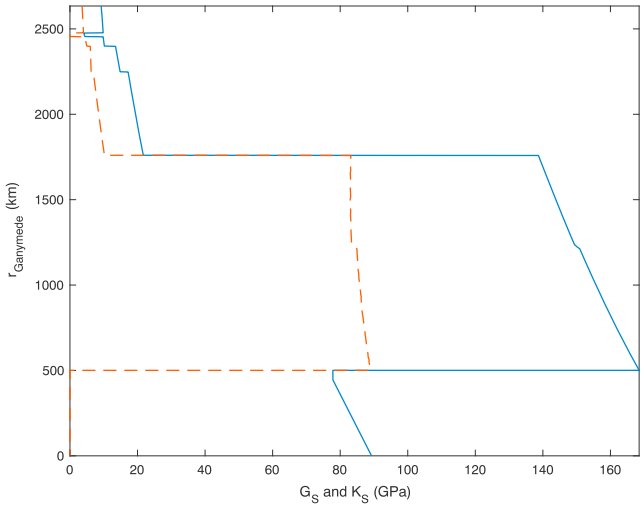

Figure 6. Ganymede: Shear and bulk moduli, G_S (dashed lines) and K_S (lines) for an ocean composition of 10 wt % $MgSO_4$ (aq) and ice Ih thickness of 157 km.

3. Results

The essential results are displayed schematically in Figure 4. For each ocean world, we display a bulk interior structure and a detailed ocean and ice structure selected from the radial profiles described below.

3.1. Ganymede

Ganymede's structure is nearly identical to those discussed by Vance et al. (2014) but with the addition of solid-state convection in the ice I layer (Table 5). For the coldest adiabatic profile, solid-state convection is nearly 4 times more efficient than conductive cooling. Figure 5 shows density as a function of pressure over the range from the surface to the water-rock interface and the corresponding temperature, sound speed, and electrical conductivity versus inferred depth for oceans with 0 and 10 wt % $MgSO_4$. For the chosen ocean salinity and core composition (Table 5), the silicate layer depth exceeds 800 km. With 10 wt % salinity, buoyant ice III occurs at the base of the ocean for the coldest adiabat. For the warmest adiabat, ice VI is also buoyant but only within the few tens of kilometers above the high-pressure ice and rock interface. Ice V is absent for the warmest case. The specified mantle heat generation is 100 GW (1 mW^{-2} at the surface or 2.5 mW^{-2} at the rock interface) at the low end of values consistent with model-based constraints on Ganymede's thermal-orbital history

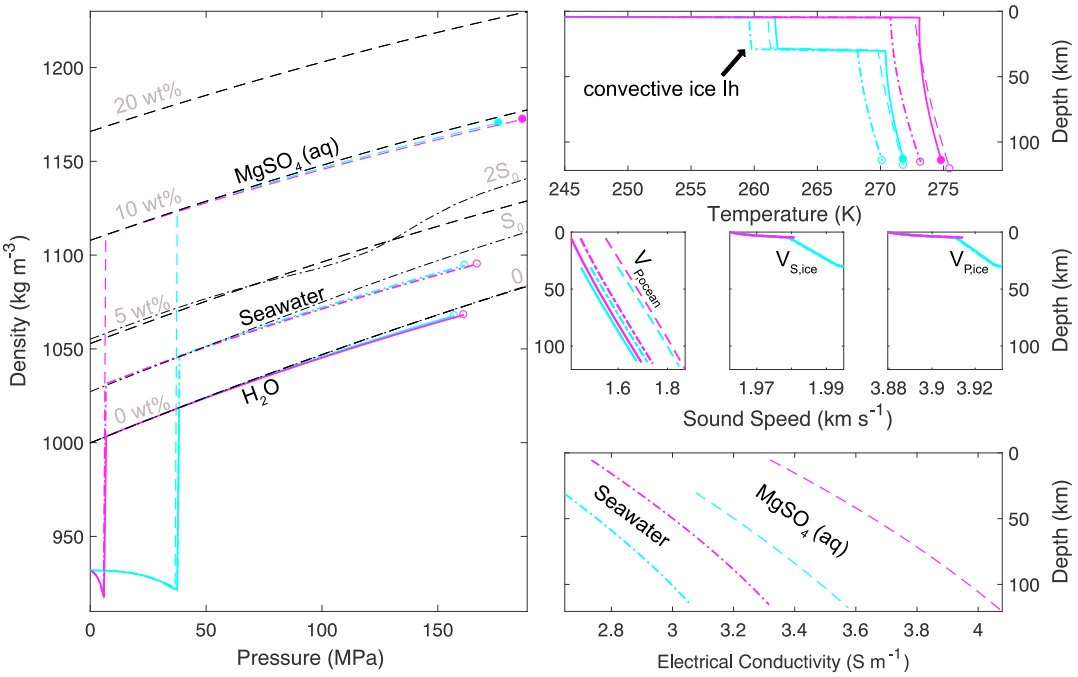

Figure 7. Europa: Oceans with 10 wt % $MgSO_4$(aq) (dashed lines), pure water (lines), and standard seawater (S_0 = 35.165 g/kg fluid, dash-dotted lines) for T_b as in Table 6. Cyans are profiles with D_{Ih} = 5 km, and magentas are colder profiles with D_{Ih} = 30 km. (left) Density versus pressure. Reference fluid densities along the melting curve for $MgSO_4$ are for {0,5,10,15} wt % and for seawater are for {0,1,2}×S_0 (S_0 = 35.16504 g/kg seawater). (right) Corresponding depth-dependent temperature (top), sound speed in the fluids and ices (fluid, V_S, V_P, middle left to right), and electrical conductivity (bottom). Circles indicate the transition to the silicate interior.

(e.g., Bland et al., 2009). The presence of a liquid core is well documented for Ganymede (Kivelson et al., 2002). We specify a 20 wt % FeS core composition consistent with the presence of melt.

Temperatures in the convecting ocean increase with depth by 0.04 K km^{-1}, or 20 K over 500 km, due to the high compressibility over 100 MPa ranges of pressure. The addition of $MgSO_4$ decreases the compressibility and decreases the adiabatic gradient.

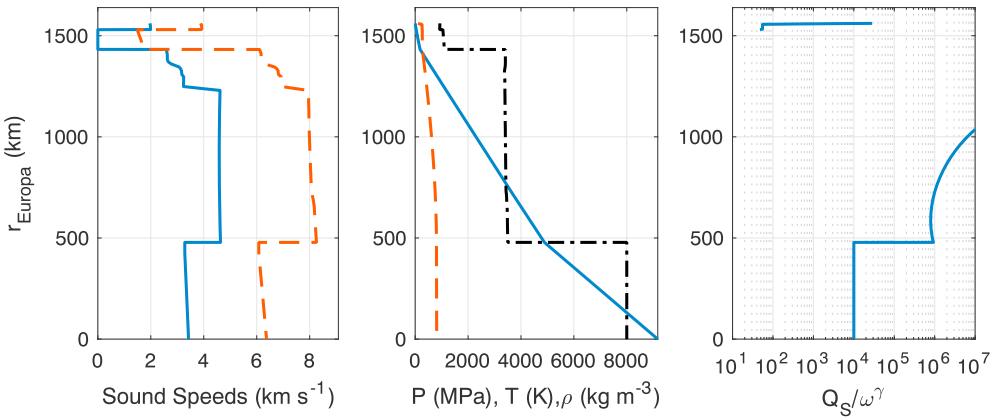

Figure 8. Europa: global interior structure for an ocean with the composition of seawater and 30 km thick ice Ih lithosphere. (left) V_S (lines) and V_P (dashed lines). (middle) Pressure (lines), temperature (dashed lines), and density (dash-dotted lines). (right) Anelasticity.

Table 6
Europa: Pyrolite Composition Containing Na_2O

$MgSO_4$	ρ_{rock} (kg m^{-3})	3,425	
10 wt %	$\rho_{rock,model}$ (kg m^{-3})	3,426	3,426
	T_b (K)	269.80	272.70
	q_b mW m^{-2}	19	123
	q_c mW m^{-2}	24	123
	D_{lh} (km)	30	5
	D_{ocean} (km)	103	131
	R_{rock} (km)	1,428	1,426
	R_{core} (km)	479	478
Water	ρ_{rock} (kg m^{-3})	3,425	
	$\rho_{rock,model}$ (kg m^{-3})	3,427	3,426
	T_b (K)	270.40	273.10
	q_b mW m^{-2}	19	119
	q_c mW m^{-2}	24	119
	D_{lh} (km)	30	5
	D_{ocean} (km)	97	124
	R_{rock} (km)	1,434	1,433
	R_{core} (km)	475	476
Seawater	ρ_{rock} (kg m^{-3})	3,425	
35.165 g/kg	$\rho_{rock,model}$ (kg m^{-3})	3,427	3,426
	T_b (K)	268.20	270.80
	q_b mW m^{-2}	18	121
	q_c mW m^{-2}	23	121
	D_{lh} (km)	30	5
	D_{ocean} (km)	99	126
	R_{rock} (km)	1,432	1,431
	R_{core} (km)	478	478

Note. $Q_{rock} = 100$ GW. $X_{FeS} = 0$ and $\rho_{core} = 8,000$ kg m^{-3}.

Sound speeds are distinct for the different ice phases and also for the freshwater and saline oceans. They differ with phase and composition by tens of km s^{-1}. Sound speeds increase with depth everywhere.

Electrical conductivity in the ocean is also distinct for the different profiles. For the two warmest adiabats, pressures exceed 400 MPa, where the downward radial derivative of electrical conductivity changes from positive to negative. This is in accord with recent investigations noting increased ion association in $MgSO_4$ (aq) above 400 MPa (Schmidt & Manning, 2017).

The bulk rock density of 3,520–3,530 kg m^{-3} (Table 3) is matched by either an anhydrous pyrolite or a saturated chondrite composition.

Shear and bulk moduli, G_S and K_S (in gigapascal), are shown in Figure 6.

3.2. Europa

Models for Europa (Figures 7 and 8 and Table 6) are adjusted through the choice of T_b to compare ice thicknesses (D_{lh}) of 5 and 30 km. For the chosen values of silicate density ($\rho_{rock} = 3,425$ kg m^{-3}) and the assumption of a pure iron core ($X_{FeS} = 0$), Europa's seafloor depth is more than 100 km below the surface.

For identical ice thicknesses, seawater suppresses the melting temperature of the ice more strongly than the chosen concentration of $MgSO_4$. Sound speeds for seawater are comparable to those of water, whereas $MgSO_4$ sound speeds are larger by more than 10%. Oceans with $MgSO_4$ have higher electrical conductivity

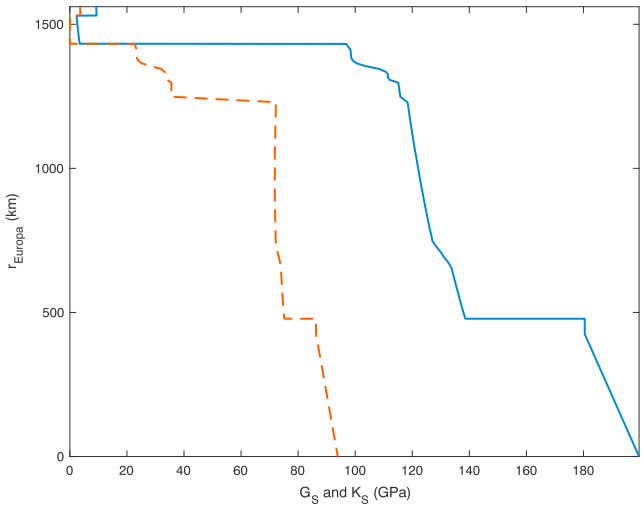

Figure 9. Europa: Shear and bulk moduli, G_S (dashed lines) and K_S (lines) for a seawater ocean composition and ice Ih thickness of 30 km.

than seawater due to both higher ionic strength and higher temperature. Reference density profiles along the melting curve for seawater are unstable above 80 MPa for salt concentrations twice the standard composition of seawater ($2S_0$, where S_0 is 35.16504 g dissolved solids per kilogram seawater, with the dissolved solids being composed of roughly 42% Na^+ and 49% Cl^- and the remainder by abundance as SO_4^{2-}, Mg^{2+}, Ca^{2+}, HCO_3^-, and lesser species; Millero et al., 2008).

Sound speeds are low in the hydrous upper portion of the rocky interior, increasing with depth due to dehydration (Figure 8). The Na_2O-bearing pyrolite provides an average rock density closest to the input value of 3,300 kg m^{-3}.

Shear and bulk moduli, G_S and K_S (in gigapascal), are shown in Figure 9.

3.3. Enceladus

Models for Enceladus (Figure 10 and Table 7) are adjusted through the choice of T_b to compare ice thicknesses of 10 and 50 km, which correspond to constraints at the hot region under the south polar Tiger Stripes and in the rest of the global ocean, respectively (Beuthe, 2016; McKinnon, 2015; Thomas et al., 2016). $MgSO_4$ is considered as an ocean constituent, despite strong inferences that the ocean has a high pH and thus is dominated by chlorides (Postberg et al., 2011; Glein et al., 2015). As with Europa, the different ocean compositions have distinct profiles in temperature, density, electrical conductivity, and sound speed. For models examining a uniform ice Ih thickness of 10 km, more consistent with thinner ice inferred at the south pole (Beuthe, 2016; Collins & Goodman, 2007; McKinnon, 2015), the depth of the silicate interior varies by up to 10 km with salinity due to the large proportional change in density of the volatile layer.

The small size of Enceladus precludes the existence of a metallic core larger than a few kilometers. Increasing the heat flux increases the average rock density of the model ($\rho_{rock,model}$). Models with thinner ice require very low densities: <2,300 kg m^{-3} for $D_{lh} = 10$ km and ≈2,350 kg m^{-3} for $D_{lh} = 20$ km. All models matching

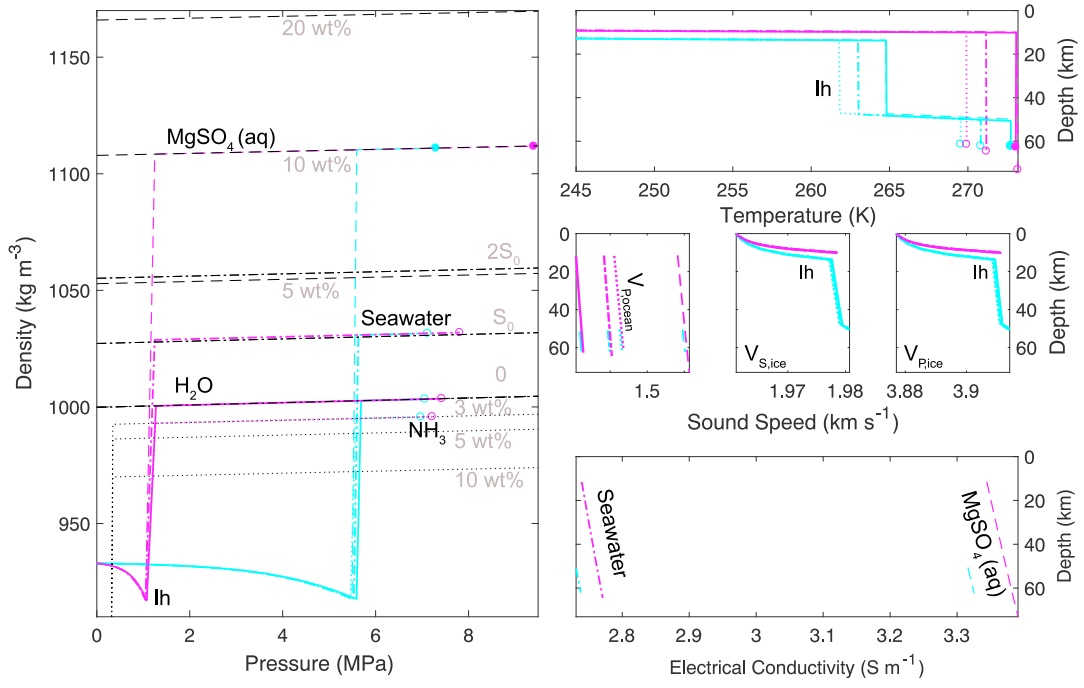

Figure 10. Enceladus: Oceans with 10 wt % $MgSO_4$(aq) (dashed lines), pure water (lines), standard seawater (dash-dotted lines), and 3 wt % NH_3 (dots) for T_b as in Table 7. Cyans are warm profiles with $D_{lh} = 10$ km, and magentas are colder profiles with $D_{lh} = 50$ km. (left) Density versus pressure. Reference densities as for Europa (Figure 7). (right) Corresponding depth-dependent temperature (top), sound speed in the fluids and ices (fluid, V_S, V_P, middle left to right), and electrical conductivity (bottom). Circles indicate the transition to the silicate interior.

Table 7
Enceladus: Anhydrous Chondrite Composition

$MgSO_4$	ρ_{rock} (kg m^{-3})	2,701	2,265
10 wt %	T_b (K)	2,699	2,691
	T_b (K)	272.72	273.12
	q_b mW m^{-2}	16	83
	q_c mW m^{-2}	10	83
	D_{lh} (km)	50	10
	D_{ocean} (km)	13	63
	R_{rock} (km)	190	179
Seawater	ρ_{rock} (kg m^{-3})	2,672	2,224
35.165g/kg	$\rho_{rock,model}$ (kg m^{-3})	2,699	2,692
	T_b (K)	270.82	271.16
	q_b mW m^{-2}	16	82
	q_c mW m^{-2}	10	82
	D_{lh} (km)	50	10
	D_{ocean} (km)	12	55
	R_{rock} (km)	190	187
Water	ρ_{rock} (kg m^{-3})	2,671	2,219
	$\rho_{rock,model}$ (kg m^{-3})	2,699	2,693
	T_b (K)	272.74	273.08
	q_b mW m^{-2}	16	81
	q_c mW m^{-2}	10	81
	D_{lh} (km)	51	10
	D_{ocean} (km)	11	53
	R_{rock} (km)	190	189
NH_3	ρ_{rock} (kg m^{-3})	2,651	2,210
3 wt %	$\rho_{rock,model}$ (kg m^{-3})	2,699	2,693
	T_b (K)	269.54	269.90
	q_b mW m^{-2}	16	81
	q_c mW m^{-2}	10	81
	D_{lh} (km)	50	10
	D_{ocean} (km)	12	51
	R_{rock} (km)	191	191

Note. $Q_{rock} = 16$ GW.

the average global ice thickness of 50 km require a low rock density of ≈2,700 kg m^{-3}. This is met by either a fully hydrous pyrolite (Table 7) or a porous, anhydrous chondrite with $\phi_1 = 0.8$, if heat production in the rock is set to the radiogenic value of 0.27 GW (Chen et al., 2014). Specifying the observed heat flux of 16 GW (Howett et al., 2011) as the heat production in the rock increases $\rho_{rock,model}$, requiring the addition of porosity ($\phi_1 = 0.5$) to match the density of the hydrous pyrolite. The average porosities for the anhydrous chondrite and hydrous pyrolite are 28% and 19%, respectively. The former value matches those obtained by Waite et al. (2017).

As shown in Figure 11, porosity introduces a depth dependence to density and to sound speeds, reducing the density by up to more than 40%. V_P and V_S are reduced by up to more than 50%. The quality factor Q_S of the rocky layer is high ($Q_S/\omega^\gamma > 10^7$).

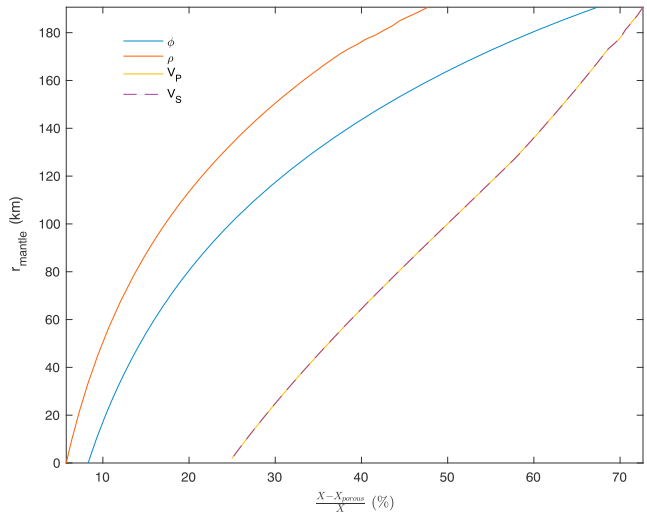

Figure 11. Enceladus: The influence of porosity (ϕ) on density (ρ), V_S (dashed lines), and V_P (lines) for an anhydrous chondrite composition. The y axis (r_{rock}) corresponds to the radial location within the rocky interior.

3.4. Titan

Titan's mean ice Ih thickness is interpreted from *Cassini-Huygens* data to be 55–80 km thick, based on the observed Schumann resonance (Béghin et al., 2012); less than 100 km based on shape, topography, and gravity (Mitri et al., 2014); and 50–200 km based on topography and admittance (Hemingway et al., 2013). We consider thicknesses in this range.

The prevalence of reduced volatiles in Titan's atmosphere and seas suggests that the ocean is reducing, which is inconsistent with the more oxidized and sulfate-rich ocean studied by Fortes et al. (2007) and Grindrod et al. (2008). Despite this inconsistency, we consider sulfate oceans due to the availability of the equation of state. We compare this with an ocean containing small amounts of ammonia (3 wt %).

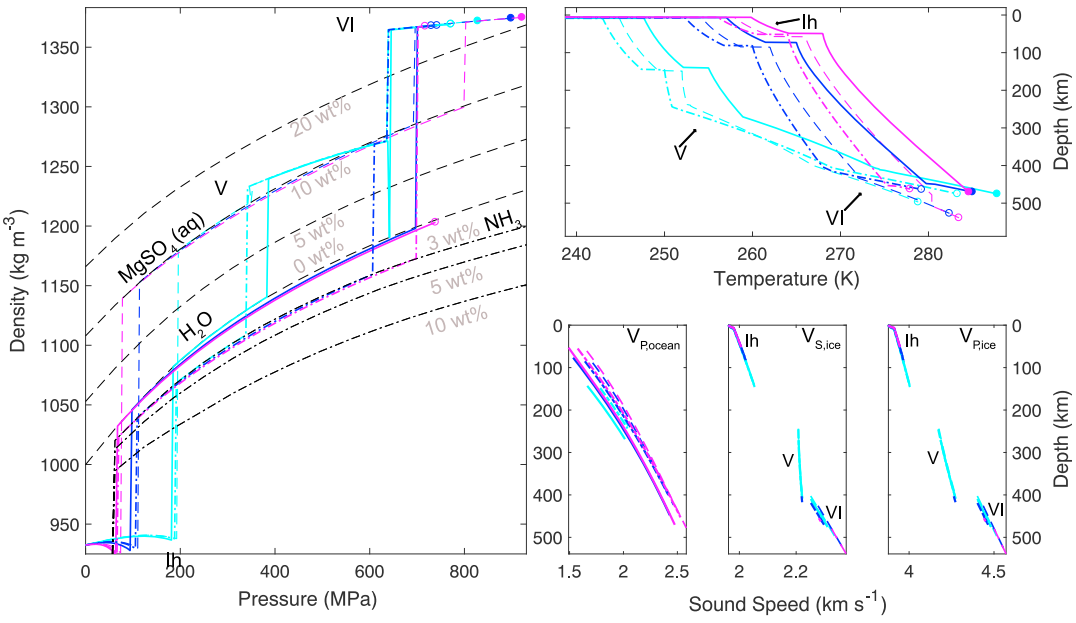

Figure 12. Titan: Oceans with 3 wt % NH_3(aq) (dash-dotted lines), pure water (lines), and $MgSO_4$ (dashed lines) for T_b as in Table 8. Magentas are warm profiles with $D_{Ih} < 60$ km, blues are modest temperature profiles with thicker ice Ih, and cyans are colder profiles with $D_{Ih} > 140$ km. (left) Density versus pressure. Reference fluid densities at {3, 5, 10} wt % for NH_3 decrease with increasing salt concentration and increase for $MgSO_4$. (right) Corresponding depth-dependent temperature (top), sound speeds in the fluids and ices (fluid, V_S, V_P, bottom left to right). Circles denote the transition to the silicate interior.

Table 8
Titan: Saturated Chondrite Composition

$MgSO_4$	ρ_{rock} (kg m^{-3})	2,616	2,545	2,524
10 wt %	$\rho_{rock,model}$ (kg m^{-3})	2,937	2,921	2,883
	T_b (K)	252	262	266
	q_b mW m^{-2}	4	8	11
	q_c mW m^{-2}	14	17	19
	D_{lh} (km)	149	86	58
	D_{ocean} (km)	91	333	403
	D_V (km)	163	-	-
	D_{VI} (km)	96	111	79
	R_{rock} (km)	2,076	2,044	2,034
Water	ρ_{rock} (kg m^{-3})	2,540	2,527	2,517
	$\rho_{rock,model}$ (kg m^{-3})	2,939	2,938	2,936
	T_b (K)	255	265	268
	q_b mW m^{-2}	4	9	13
	q_c mW m^{-2}	14	18	20
	D_{lh} (km)	141	74	50
	D_{ocean} (km)	130	369	420
	D_V (km)	140	-	-
	D_{VI} (km)	67	27	2
	R_{rock} (km)	2,097	2,104	2,103
NH_3	ρ_{rock} (kg m^{-3})	2,531	2,523	2,519
3 wt %	$\rho_{rock,model}$ (kg m^{-3})	2,939	2,938	2,937
	T_b (K)	250	260	264
	q_b mW m^{-2}	4	8	12
	q_c mW m^{-2}	13	17	19
	D_{lh} (km)	146	82	52
	D_{ocean} (km)	100	321	396
	D_V (km)	164	16	-
	D_{VI} (km)	68	46	15
	R_{rock} (km)	2,097	2,110	2,112

Note. $Q_{rock} = 12$ GW.

Results for Titan are shown in Figure 12 and Table 8. A metallic core is not permitted by the high gravitational moment of inertia. In fact, even omitting a central high-density core, neither the saturated chondrite model nor the pyrolite model matches the mean rock density, $\rho_{rock} \approx 2,600$ kg m^{-3}. The saturated pyrolite composition comes closest, at around 2,940 kg m^{-3}. Heat production in the rocky interior is set to 12 GW (0.1 mW m^{-2}); higher values increase the rock density by 50–100 kg m^{-3}. For the pure water ocean (solid lines), ice phases V and VI are present, except in the warmest cases. The 3 wt % NH_3 ocean has a lower density and slightly larger adiabatic temperature gradient (0.1 K km^{-1} versus 0.07 K km^{-1} for the $MgSO_4$ case). The lower fluid compressibility corresponds to a higher sound speed. For the warmest models ($T_b = 264$ and 268 K), the ammonia and water oceans have little or no high-pressure ice. The higher densities of the $MgSO_4$ oceans increase the depth of the silicate transition needed to match the gravity data and thus result in thicker high-pressure ice layers.

Shear and bulk moduli, G_S and K_S (in gigapascal), are shown in Figure 13. The average value of K_S in the rock is about 100 GPa, half the value assumed by Mitri et al. (2014). The average value of G_S of about 50 GPa is less than the 70 GPa value chosen by Mitri et al. (2014).

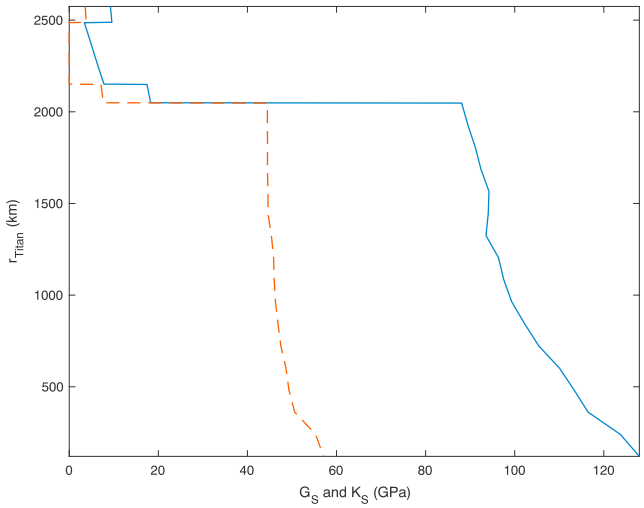

Figure 13. Titan: Shear and bulk moduli, G_S (dashed lines), and K_S (lines) for an ocean composition of 10 wt % $MgSO_4$ (aq) and ice Ih thickness of 86 km.

3.5. Callisto

For Callisto, we consider ice thicknesses exceeding 100 km (Table 9). For simplicity we do not modify the parameterization of solid-state convection to accommodate a fully stagnant lid (McKinnon, 2006). We consider oceans with 0 and 10 wt % $MgSO_4$. Figure 14 shows profiles for both the reported value of Callisto's gravitational moment of inertia ($C/MR^2 = 0.3549 \pm 0.0042$; Schubert et al., 2004, Figure 14) and a value that is 10% smaller ($C/MR^2 = 0.32$; Gao & Stevenson, 2013).

Table 9
Callisto: Saturated Pyrolite Composition

$MgSO_4$	ρ_{rock} (kg m^{-3})	3,118	3,054
10 wt %	$\rho_{rock,model}$ (kg m^{-3})	3,088	3,071
	T_b (K)	250	255.70
	q_b mW m^{-2}	4	5
	q_c mW m^{-2}	16	18
	D_{lh} (km)	130	100
	D_{ocean} (km)	20	132
	D_{III} (km)	46	-
	D_V (km)	50	20
	R_{rock} (km)	2,165	2,158
Water	ρ_{rock} (kg m^{-3})	3,094	3,077
	$\rho_{rock,model}$ (kg m^{-3})	3,089	3,085
	T_b (K)	253.10	257.40
	q_b mW m^{-2}	4	5
	q_c mW m^{-2}	17	18
	D_{lh} (km)	120	100
	D_{ocean} (km)	62	139
	D_{III} (km)	16	-
	D_V (km)	46	6
	R_{rock} (km)	2,166	2,166

Note. $Q_{rock} = 130$ GW.

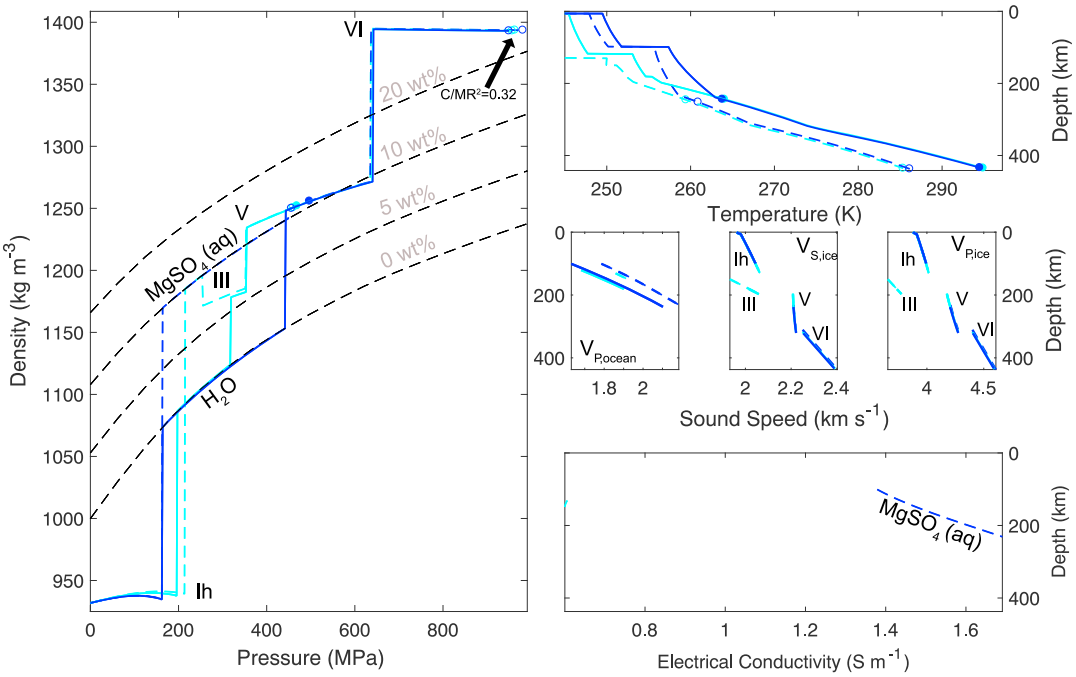

Figure 14. Callisto: Oceans with 10 wt % $MgSO_4$(aq) (dashed lines), pure water (lines), and standard seawater (dash-dotted lines) for T_b as in Table 9. Blues are warm profiles with $D_{lh} < 30$ km, cyans are modest temperature profiles with thicker ice Ih, and magentas are colder profiles with $D_{lh} > 130$ km. (left) Density versus pressure. (right) Corresponding depth-dependent temperature (top), sound speed in the fluids and ices (fluid, V_S, V_P, middle left to right), and electrical conductivity (bottom). Circles indicate the transition to the silicate interior. Greater silicate depths and pressures, and the presence of ice V, are also shown for the assumption of $C/MR^2 = 0.32$.

Table 10
Callisto With $C/MR^2 = 0.32$ and Pyrolite Composition Containing Na_2O

$MgSO_4$	ρ_{rock} (kg m^{-3})	3,525	
10 wt %	$\rho_{rock,model}$ (kg m^{-3})	3,526	3,527
	T_b (K)	250	255.70
	q_b mW m^{-2}	4	5
	q_c mW m^{-2}	16	18
	D_{lh} (km)	130	100
	D_{ocean} (km)	20	132
	D_{III} (km)	46	-
	D_V (km)	120	79
	D_{VI} (km)	122	129
	R_{rock} (km)	1,972	1,971
	R_{core} (km)	592	568
Water	ρ_{rock} (kg m^{-3})	3,525	
	$\rho_{rock,model}$ (kg m^{-3})	3,524	3,524
	T_b (K)	253.10	257.40
	q_b mW m^{-2}	4	5
	q_c mW m^{-2}	17	18
	D_{lh} (km)	120	100
	D_{ocean} (km)	62	139
	D_{III} (km)	16	-
	D_V (km)	121	83
	D_{VI} (km)	118	116
	R_{rock} (km)	1,973	1,973
	R_{core} (km)	598	607

Note. $Q_{rock} = 110$ GW. $X_{FeS} = 0$, and $\rho_{core} = 8,000$ kg m^{-3}.

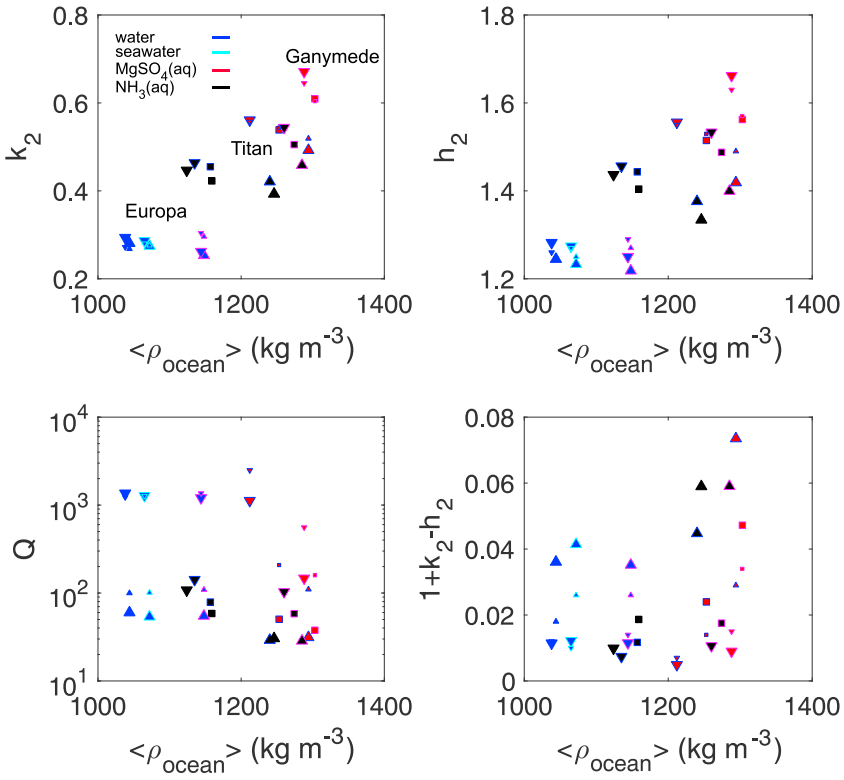

Figure 15. Tidal deformation properties (top left) k_2, (top right) h_2, (bottom left) Q, and (bottom right) $1 + k_2 - h_2$ versus mean ocean density for Europa, Titan, and Ganymede based on the interior models described above. The thickest ice models are denoted by a triangle and the thinnest by an inverted triangle. Ocean compositions are denoted by the marker outline colors; k_2 and h_2 increase with density. Large and small markers are computations using Andrade and Maxwell rheological models, respectively.

The currently accepted higher value of C/MR^2 precludes the presence of a metallic core and requires a low silicate density around 3,100 kg m^{-3} (Table 9), most consistent with the saturated pyrolite composition. Rock interface depths of less than ~250 km are required. Ice VI does not occur. Buoyant ice III is present for the coldest oceans containing both pure water and salt.

The smaller value of C/MR^2, corresponding to a possible error intrinsic in the assumption that Callisto is hydrostatic, would require silicate depths similar to Ganymede's (Table 10). An iron core is required and is specified as pure (γ) Fe. Rock densities are best fit by the anhydrous pyrolite composition. Ice VI is always present, and buoyant ice III is present in the coldest model that includes salts.

3.6. Tidal Deformation

The tidal responses of Europa, Ganymede, and Titan are shown in Figure 15. We assume a reference viscosity of 10^{13} Pa s for ice Ih. For both Maxwell and Andrade rheologies (Castillo-Rogez et al., 2011; Dumoulin et al., 2017) the response increases with body size and depends mainly on the ocean's density and the thickness of the outer ice shell. This is consistent with results from previous studies (Kamata et al., 2015; Mitri et al., 2014; Moore & Schubert, 2003; Steinbrügge et al., 2015; Tobie et al., 2005). The structure underneath the ocean has less of an effect on the tidal deformation properties. The dissipation Q and tilt factor $1+k_2-h_2$ depend strongly on the ice thickness. Specifically, the combination of a denser ocean and a thinner ice shell corresponds to larger Love numbers, as also noted by Mitri et al. (2014). Computations using the Maxwell rheology (Kamata et al., 2015) have a narrower range of values for k_2, h_2, and $1 + k_2 - h_2$ than models with the Andrade rheology and tend to generate larger values of Q.

4. Discussion

Combinations of ocean salinity, bulk density, density structure, and ice thicknesses provide synergistic constraints on the properties of the constituent materials, which must be logically consistent (as discussed, e.g., by Grasset et al., 2013). For example, global heat fluxes—which have yet to be measured directly—couple with salinity to determine which crystalline forms of ice are present in what amounts. The radial profiles in pressure and density determine whether these ices will sink or float.

Applying our model to known icy ocean worlds allows us to compare them. The low-density rocky components of Titan and Enceladus contrast sharply with those of the higher-density interiors of the Galilean satellites. It may be that both Saturnian satellites retained much more volatile carbon and nitrogen than is accounted for by the pyrolite and chondrite mineralogies studied here.

4.1. Means for Investigating Habitability

4.1.1. Europa

The seawater and $MgSO_4$ oceans examined for Europa span oxidized and low pH to reduced and high pH, as modeled by Zolotov (2008). For similar ice thicknesses, the higher-pH seawater ocean has a lower temperature, electrical conductivity, density, and sound speed. The electrical conductivity and density will be constrained by gravity and electromagnetic experiments on the JUICE (Grasset et al., 2013) and Europa (Pappalardo et al., 2016) missions, in combination with radar sounding and topographic imaging. A subsequent seismic experiment could address any degeneracies in the inferred ocean density and electrical conductivity by measuring the oceanic sound speed. Thermal and radar mapping will establish the existence and characteristics of solid-state convection, providing additional prior constraints for a follow-on seismic investigation. With this background established, it may be possible to determine the extent of aqueous alteration and sedimentation at the seafloor (Vance, Tsai, et al., 2016).

4.1.2. Enceladus

The silicate interior of Enceladus controls the extent of water-rock interaction, including the production of hydrogen identified in south polar plume materials (Waite et al., 2017). Though it has been suggested that the rocky core of Enceladus must be fully hydrated (Vance et al., 2007; Vance, Hand, et al., 2016) as per the hydrous pyrolite model used here, the low pressures at Enceladus also permit an anhydrous chondrite composition with high porosities consistent with those of the regolith of Earth's Moon. A transition from anhydrous to hydrous rock via water-rock interactions could explain the evident present-day production of hydrogen (Hsu et al., 2015) and might be consistent with recent activation or even formation of Enceladus (Ćuk et al., 2016). Regardless of the hydration state, the inferred high heat production in Enceladus (Howett et al., 2011) requires some degree of porosity to match the required density for both the pyrolite and chondrite compositions.

Electromagnetic and seismic measurements could evaluate the extent and role of fluids and gases in south polar plume eruptions (Hsu et al., 2015; Kite & Rubin, 2016; Postberg et al., 2011). By analogy with investigations of geysers and volcanoes on Earth, a seismic experiment could reveal the flow rates, compositions, and geometry of plumes on Enceladus (Vance et al., 2017, Stäehler et al. under revision). Such an experiment might also measure the porosity of the rocky interior and search for a small metallic core.

4.1.3. Titan

Titan's ocean must have a bulk density >1,200 kg m^{-3} if the large value of the measured tidal Love number ($k_2 > 0.6$) is correct (Mitri et al., 2014). In the study of Mitri et al. (2014), following the approach of Lefevre et al. (2014), the ocean density was arbitrarily increased, assuming uniform density increments throughout the ocean with reference to a pure water case (Choukroun & Grasset, 2007). No direct link with the ocean composition was possible then. In the present study, we show that the 10 wt % $MgSO_4$ ocean meets this requirement. As noted above, a reducing ocean dominated instead by chlorides can obtain similar large densities. A saline ocean is not expressly required by the current uncertainty in the Love number ($k_2 = 0.637 \pm 0.220$), which permits densities as low as 1,100 kg m^{-3}, consistent with the pure water or 3 wt % cases studied here. If k_2 is in fact larger than 0.6, our models show that a dense, salty ocean and thin ice require a high heat flux, exceeding 800 GW (10 mW m^{-2}; Table 8). Such a high heat flux would be consistent with recent geological activation of Titan, perhaps concurrent with the formation of Saturn's rings (Ćuk et al., 2016).

A dense ocean and thin ice only worsen the problem of accounting for the low density (2,600 kg m^{-3}) of Titan's rocky interior. It seems likely that Titan is weakly differentiated, highly porous, or both. Alternatively, a differentiated Titan with a small metallic core ($R < 400$ km) would be permitted by the gravitational constraints

if the low-density layer under the ocean can be explained. If Titan's ice is indeed thin and if the ocean has a low salinity, high-pressure ices may be minimal or absent entirely.

4.1.4. Ganymede

High heat flux and ice Ih as thin as ~10 km are in accord with the formation of grooved terrains on the surface (Hammond & Barr, 2014). However, these would require tidal heating. At present, tidal heating is probably negligible (e.g., Bland & McKinnon, 2015).

In general, the presence of high-pressure ice phases V, VI, and III should slow the loss of heat by inhibiting efficient convection and releasing latent heat upon freezing. However, two-phase convection seems likely in high-pressure ices (Kalousová et al., 2018). Accounting for salinity should only enhance the efficiency of cooling and transport. Ices III and VI can become dynamically unstable in the presence of aqueous solutions containing high salt concentrations (Journaux et al., 2013; Vance et al., 2014). For the chosen $MgSO_4$ concentration of 10 wt %, ice V may also become buoyant in the vicinity the transition to ice VI. The lack of a dynamically stable upper solid layer in the case of ice III might suggest efficient overturning of upward snows that would hasten the cooling of Ganymede's interior through the exchange of latent heat.

The planned JUICE mission (Grasset et al., 2013) will constrain the global density structure of Ganymede, its ice Ih thickness, and the conductance of its ocean. Using this prior information, a seismic investigation could reveal the radial structures of the ices and search for any liquids within and between those layers, including the abundance of liquids at the water-rock interface.

4.1.5. Callisto

Poor constraints on Callisto's density structure mean that its ocean can be either Europa like, less than 250 km deep, and containing scarce or no high-pressure ices or Titan like, with seafloor pressures approaching 800 MPa and the presence of ices V and VI. The inactive surface seems most consistent with the undifferentiated case; else, it is difficult to conceive of how Callisto would have cooled within a few hundred million years after fully differentiating. In either case, the fully stagnant surface suggests that the ocean is nearly frozen and so has a near-eutectic composition. This should lead to a high electrical conductivity. Buoyant ice III may be present, unless the ocean contains strong freezing suppressants such as ammonia or methanol.

4.2. Limitations in Available Thermodynamic Properties

Fluids: Evaluating the differences between high- and low-pH oceans in larger satellites (chloride versus sulfate; Zolotov & Kargel, 2009) requires high-pressure thermodynamic data for aqueous NaCl and mixtures with sulfates, including the associated melting point suppression of ices. In the present work, we are limited to comparing seawater as a proxy for NaCl solutions, when in fact standard seawater contains {1.28372,2.71235} g Mg,SO_4} per kg solution of Millero et al. (2008). Some of the needed information for single-component solutions is available at pressures relevant to watery exoplanets (Journaux et al., 2013; Mantegazzi et al., 2013), but crucial measurements in the 0.1–1 GPa range of pressures are lacking. As a result, we cannot evaluate near-eutectic salinities that may occur and which would have the greatest influence on the stability of high-pressure ices. Assuming zero error in bulk density, moment of inertia, and radius, the present predictions of ice thicknesses and layer depths are uncertain by ~10 km or more due to uncertainties in the melting temperatures of ices at elevated pressure.

A more rigorous treatment of conductivity should evaluate the limitations of available theory (Marshall, 1987). Laboratory electrical conductivity measurements could test the extrapolations to high salinity assumed herein.

Solids: To accurately interpret seismic measurements in terrestrial glaciers and in ocean worlds, sound speed measurements are needed in ices Ih, II, III, V, and VI at temperatures other than −35°C. This would enable the development of thermodynamic properties comparable to those available for fluids and more comprehensive predictions of the melting curves of ices in the presence of salts. The present work is also limited by the scarcity of thermodynamic information regarding impurities in solid phases. Recent work suggests a pivotal role of clathrates (Choukroun et al., 2010; Sohl et al., 2010) in regulating global volatile inventories and of trapped ions within ices (Fortes & Choukroun, 2010; Journaux et al., 2013, 2017) in controlling buoyancy. Further work incorporating properties of these materials is needed in order to understand whether geophysical measurements can discern such effects.

More detailed consideration of the effects of rocks and metals is needed. The present work explored a small set of parameters in favor of focusing on fluids and ices closer to the surface. Future work will need to address

inconsistencies in the thermodynamic data. In the present work, for example, silicate melts occurred in interior models that included heat production values in the range of plausible radiogenic estimates (e.g., 250 GW for Europa; Vance et al., 2007). We did not include analyses of those results because of the possible occurrence of melt at pressures exceeding 1 GPa that showed unstable behavior, as noted in the Perple_X documentation, in the form of densities exceeding 3,000 kg m^{-3}.

5. Conclusions

Calculations of the radial compositional structure of icy ocean worlds demonstrate the utility of geophysical measurements for investigating habitability. We have focused on the relation between ice thickness and ocean composition, building on prior work (Vance et al., 2014) to illustrate the unique 1-D structures arising from the combination of melting point suppression and density in single-component oceans containing aqueous $MgSO_4$, NaCl (as seawater), and NH_3. Europa's ocean pH may be further constrained by seismology, supplemented by gravity, radar, electromagnetic, and compositional measurements by the planned Europa Clipper mission. Accounting for detailed rock properties reveals that a high porosity for the interior of Enceladus is required to accommodate for the measured density structure and heat flux. Titan's ocean may be dense and saline, but this requires an as-yet unexplained low-density layer in the solid interior. Titan and Callisto may lack high-pressure ices altogether.

The seismic noise environment and wave propagation properties of icy ocean worlds can be investigated using the results described here (e.g., Panning et al., 2018; Stähler et al., 2018), as can the tidal response and electromagnetic properties and their responses to external forcing.

The accuracy of the model results is limited by the availability of equation-of-state data under conditions occurring in icy ocean worlds. Further measurements are needed of ice and rock melting points in the presence of aqueous solutions and sound speeds and electrical conductivities. Measurements are needed especially in aqueous solutions at elevated salt concentration, low temperature, and high pressure. Further measurements of sound velocities in ices would aid both seismic and geodynamic modeling.

Future work should consider the influence of the rocky interior and partitioning of elements between the core, mantle, and ocean by considering different early planetary formation events, which would result in different mineral and elemental compositions, hydration states, porosity, and heat content. Future work focusing on specific worlds can make use of new thermodynamic data for fluids and solids to evaluate the couplings between rock and ocean composition and the presence of various ice phases. Similarly, the properties of the iron-rich core can be varied in concert with the rock composition to explore the parameter space of heat and metal content in the cores of Europa, Ganymede, and possibly Titan.

Acknowledgments
We thank Jurrien Knibbe and an anonymous reviewer for thoughtful and detailed reviews that improved the quality of this paper. The PlanetProfile model and applications described in this work are available online (Vance, 2017). Support for its use may be obtained from SDV via email. Work by JPL co-authors was partially supported by strategic research and technology funds from the Jet Propulsion Laboratory, Caltech, and by the Icy Worlds node of NASA's Astrobiology Institute (13-13NAI7_2-0024). G. T. acknowledges supports from CNES for the ESA JUICE mission and the NASA Europa Clipper mission and for the project ANR OASIS. R. L. acknowledges the support of NASA Outer Planets Research grant NNX13AK97G "Physical Processes in Titan's Seas." S. C. S. was supported by grant SI1538/4-1 of Deutsche Forschungsgemeinschaft DFG. S. D. V. acknowledges the support of NASA Outer Planets Research grant NNH12ZDA001N "Solution Thermochemistry Relevant to Outer Planets and Satellites." No conflicts of interest are identified associated with this work. A part of the research was carried out at the Jet Propulsion Laboratory, California Institute of Technology, under a contract with the National Aeronautics and Space Administration.

References

Anderson, J. (2001). Shape, mean radius, gravity field, and interior structure of Callisto. *Icarus*, *153*(1), 157–161. https://doi.org/10.1006/icar.2001.6664

Anderson, J. D. (1998). Europa's differentiated internal structure: Inferences from four Galileo encounters. *Science*, *281*(5385), 2019–2022. https://doi.org/10.1126/science.281.5385.2019

Anderson, J. D., Lau, E. L., Sjogren, W. L., Schubert, G., & Moore, W. B. (1996). Gravitational constraints on the internal structure of Ganymede. *Nature*, *384*(6609), 541–543. https://doi.org/10.1038/384541a0

Andersson, O., & Inaba, A. (2005). Thermal conductivity of crystalline and amorphous ices and its implications on amorphization and glassy water. *Physical Chemistry Chemical Physics*, *7*(7), 1441. https://doi.org/10.1039/b500373c

Béghin, C., Randriamboarison, O., Hamelin, M., Karkoschka, E., Sotin, C., Whitten, R. C., … Simões, F., (2012). Analytic theory of Titan's Schumann resonance: Constraints on ionospheric conductivity and buried water ocean. *Icarus*, *218*(2), 1028–1042. https://doi.org/10.1016/j.icarus.2012.02.005

Bell, R. E., Blankenship, D. D., Finn, C. A., Morse, D. L., Scambos, T. A., Brozena, J. M., & Hodge, S. M. (1998). Influence of subglacial geology on the onset of a West Antarctic ice stream from aerogeophysical observations. *Nature*, *394*(6688), 58–62. https://doi.org/10.1038/27883

Beuthe, M. (2016). Crustal control of dissipative ocean tides in Enceladus and other icy moons. *Icarus*, *280*, 278–299. https://doi.org/10.1016/j.icarus.2016.08.009

Bland, M. T., & McKinnon, W. B. (2015). Forming Ganymede's grooves at smaller strain: Toward a self-consistent local and global strain history for Ganymede. *Icarus*, *245*, 247–262. https://doi.org/10.1016/j.icarus.2014.09.008

Bland, M. T., Showman, A. P., & Tobie, G. (2009). The orbital-thermal evolution and global expansion of Ganymede. *Icarus*, *200*(1), 207–221. https://doi.org/10.1016/j.icarus.2008.11.016

Bruzzone, L., Plaut, J. J., Alberti, G., Blankenship, D. D., Bovolo, F., Campbell, B. A., … Seu, R. (2013). Rime: Radar for icy moon exploration. In *2013 IEEE International Geoscience and Remote Sensing Symposium (IGARSS)*, IEEE, Melbourne, VIC, Australia (pp. 3907–3910).

Cammarano, F., Lekic, V., Manga, M., Panning, M., & Romanowicz, B. (2006). Long-period seismology on Europa: 1. Physically consistent interior models. *Journal of Geophysical Research*, *111*, E12009. https://doi.org/10.1029/2006JE002710

Cammarano, F., Tackley, P., & Boschi, L. (2011). Seismic, petrological and geodynamical constraints on thermal and compositional structure of the upper mantle: Global thermochemical models. *Geophysical Journal International*, *187*, 1301–1318. https://doi.org/10.1111/j.1365-246X.2011.05223.x

Carlson, R. L. (2014). The influence of porosity and crack morphology on seismic velocity and permeability in the upper oceanic crust. *Geochemistry, Geophysics, Geosystems*, *15*, 10–27. https://doi.org/10.1002/2013GC004965

Castillo-Rogez, J. C., Efroimsky, M., & Lainey, V. (2011). The tidal history of Iapetus: Spin dynamics in the light of a refined dissipation model. *Journal of Geophysical Research*, *116*, E09008. https://doi.org/10.1029/2010JE003664

Chen, E., Nimmo, F., & Glatzmaier, G. (2014). Tidal heating in icy satellite oceans. *Icarus*, *229*, 11–30. https://doi.org/10.1016/j.icarus.2013.10.024

Choblet, G., Tobie, G., Sotin, C., Kalousová, K., & Grasset, O. (2017). Heat transport in the high-pressure ice mantle of large icy moons. *Icarus*, *285*, 252–262. https://doi.org/10.1016/j.icarus.2016.12.002

Choukroun, M., & Grasset, O. (2007). Thermodynamic model for water and high-pressure ices up to 2.2 GPa and down to the metastable domain. *The Journal of Chemical Physics*, *127*(12), 124506. https://doi.org/10.1063/1.2768957

Choukroun, M., & Grasset, O. (2010). Thermodynamic data and modeling of the water and ammonia-water phase diagrams up to 2.2 GPa for planetary geophysics. *The Journal of Chemical Physics*, *133*(14), 144502. https://doi.org/10.1063/1.3487520

Choukroun, M., Grasset, O., Tobie, G., & Sotin, C. (2010). Stability of methane clathrate hydrates under pressure: Influence on outgassing processes of methane on Titan. *Icarus*, *205*(2), 581–593. https://doi.org/10.1016/j. icarus.2009.08.011

Christensen, N. I. (1989). Chapter 32: Pore pressure, seismic velocities, and crustal structure. *Geophysical Framework of the Continental United States*, *172*, 783–798. https://doi.org/10.1130/mem172-p783

Collins, G. C., & Goodman, J. C. (2007). Enceladus' south polar sea. *Icarus*, *189*(1), 72–82. https://doi.org/10.1016/j.icarus.2007.01.010

Connolly, J. (2005). Computation of phase equilibria by linear programming: A tool for geodynamic modeling and its application to subduction zone decarbonation. *Earth and Planetary Science Letters*, *236*(1–2), 524–541. https://doi.org/10.1016/j.epsl.2005.04.033

Connolly, J. A. D. (2009). The geodynamic equation of state: What and how. *Geochemistry, Geophysics, Geosystems*, *10*, Q10014. https://doi.org/10.1029/2009GC002540

Ćuk, M., Dones, L., & Nesvorný, D. (2016). Dynamical evidence for a late formation of Saturn's moons. *The Astrophysical Journal*, *820*(2), 97. https://doi.org/10.3847/0004-637x/820/2/97

Darot, M., & Reuschlé, T. (2000). Effect of pore and confining pressures on V_p in thermally pre-cracked granites. *Geophysical Research Letters*, *27*(7), 1057–1060. https://doi.org/10.1029/1999GL008414

Deschamps, F., & Sotin, C. (2001). Thermal convection in the outer shell of large icy satellites. *Journal of Geophysical Research*, *106*(E3), 5107–5121. https://doi.org/10.1029/2000JE001253

Diez, A. (2013). Effects of cold glacier ice crystal anisotropy on seismic data (PhD thesis), Geophysikalisches Institut (GPI).

Dumoulin, C., Tobie, G., Verhoeven, O., Rosenblatt, P., & Rambaux, N. (2017). Tidal constraints on the interior of Venus. *Journal of Geophysical Research: Planets*, *122*, 1338–1352. https://doi.org/10.1002/2016JE005249

Durham, W. B., Kirby, S. H., & Stern, L. A. (1997). Creep of water ices at planetary conditions: A compilation. *Journal of Geophysical Research*, *102*(E7), 16,293–16,302. https://doi.org/10.1029/97JE00916

Fortes, A., Grindrod, P., Trickett, S., & Vocadlo, L. (2007). Ammonium sulfate on Titan: Possible origin and role in cryovolcanism. *Icarus*, *188*(1), 139–153. https://doi.org/10.1016/j.icarus.2006.11.002

Fortes, A. D., & Choukroun, M. (2010). Phase behaviour of ices and hydrates. *Space Science Reviews*, *153*(1–4), 185–218. https://doi.org/10.1007/s11214-010-9633-3

Gagnon, R. E., Kiefte, H., Clouter, M. J., & Whalley, E. (1988). Pressure dependence of the elastic constants of ice Ih to 2.8 kbar by Brillouin spectroscopy. *The Journal of Chemical Physics*, *89*(8), 4522–4528. https://doi.org/10.1063/1.454792

Gagnon, R. E., Kiefte, H., Clouter, M. J., & Whalley, E. (1990). Acoustic velocities and densities of polycrystalline ice Ih, II, III, V, and VI by Brillouin spectroscopy. *The Journal of Chemical Physics*, *92*(3), 1909–1914. https://doi.org/10.1063/1.458021

Gao, P., & Stevenson, D. J. (2013). Nonhydrostatic effects and the determination of icy satellites' moment of inertia. *Icarus*, *226*(2), 1185–1191. https://doi.org/10.1016/j.icarus.2013.07.034

Glein, C. R., Baross, J. A., & Waite, J. H. (2015). The pH of Enceladus' ocean. *Geochimica et Cosmochimica Acta*, *162*, 202–219. https://doi.org/10.1016/j.gca.2015.04.017

Goldsby, D. L., & Kohlstedt, D. L. (2001). Superplastic deformation of ice: Experimental observations. *Journal of Geophysical Research*, *106*(B6), 11,017–11,030. https://doi.org/10.1029/2000JB900336

Gomi, H., Ohta, K., Hirose, K., Labrosse, S., Caracas, R., Verstraete, M. J., & Hernlund, J. W. (2013). The high conductivity of iron and thermal evolution of the Earth's core. *Physics of the Earth and Planetary Interiors*, *224*, 88–103. https://doi.org/10.1016/j.pepi.2013.07.010

Grasset, O., Dougherty, M., Coustenis, A., Bunce, E., Erd, C., Titov, D., … Van Hoolst, T. (2013). Jupiter icy moons explorer (juice): An ESA mission to orbit Ganymede and to characterise the Jupiter system. *Planetary and Space Science*, *78*, 1–21. https://doi.org/10.1016/j.pss.2012.12.002

Grima, C., Blankenship, D. D., & Schroeder, D. M. (2015). Radar signal propagation through the ionosphere of Europa. *Planetary and Space Science*, *117*, 421–428. https://doi.org/10.1016/j.pss.2015.08.017

Grindrod, P., Fortes, A., Nimmo, F., Feltham, D., Brodholt, J., & Vocadlo, L. (2008). The long-term stability of a possible aqueous ammonium sulfate ocean inside Titan. *Icarus*, *197*(1), 137–151. https://doi.org/10.1016/j.icarus.2008.04.006

Hammond, N. P., & Barr, A. C. (2014). Formation of Ganymede's grooved terrain by convection-driven resurfacing. *Icarus*, *227*, 206–209. https://doi.org/10.1016/j.icarus.2013.08.024

Han, S.-C., Schmerr, N., Neumann, G., & Holmes, S. (2014). Global characteristics of porosity and density stratification within the lunar crust from GRAIL gravity and lunar orbiter laser altimeter topography data. *Geophysical Research Letters*, *41*, 1882–1889. https://doi.org/10.1002/2014GL059378

Hand, K., & Chyba, C. (2007). Empirical constraints on the salinity of the European ocean and implications for a thin ice shell. *Icarus*, *189*(2), 424–438. https://doi.org/10.1016/j.icarus.2007.02.002

Hand, K. P., Murray, A. E., Garvin, J. B., Brinckerhoff, W. B., Christner, B. C., Edgett, K. S., … Hoehler, T. M. (2017). Report of the Europa Lander Science Definition Team: Jet Propulsion Laboratory, California Institute of Technology.

Helffrich, G., & Connolly, J. (2009). Physical contradictions and remedies using simple polythermal equations of state. *American Mineralogist*, *94*(11–12), 1616–1619. https://doi.org/10.2138/am.2009.3262

Hemingway, D., Nimmo, F., Zebker, H., & less, L. (2013). A rigid and weathered ice shell on Titan. *Nature*, *500*(7464), 550–552. https://doi.org/10.1038/nature12400

Hogenboom, D. (1995). Magnesium sulfate-water to 400 MPa using a novel piezometer: Densities, phase equilibria, and planetological implications. *Icarus*, *115*(2), 258–277. https://doi.org/10.1006/icar.1995.1096

Holland, T. J. B., & Powell, R. (2011). An improved and extended internally consistent thermodynamic dataset for phases of petrological interest, involving a new equation of state for solids. *Journal of Metamorphic Geology*, *29*(3), 333–383. https://doi.org/10.1111/j.1525-1314.2010.00923.x

Howett, C. J. A., Spencer, J. R., Pearl, J., & Segura, M. (2011). High heat flow from Enceladus' south polar region measured using 10–600 cm^{-1} Cassini/CIRS data. *Journal of Geophysical Research*, *116*, E03003. https://doi.org/10.1029/2010JE003718

Hsu, H.-W., Postberg, F., Sekine, Y., Shibuya, T., Kempf, S., Horányi, M., … Srama, R. (2015). Ongoing hydrothermal activities within Enceladus. *Nature*, *519*(7542), 207–210. https://doi.org/10.1038/nature14262

Huang, X., Xu, Y., & Karato, S.-I. (2005). Water content in the transition zone from electrical conductivity of wadsleyite and ringwoodite. *Nature*, *434*(7034), 746–749. https://doi.org/10.1038/nature03426

Iess, L., Jacobson, R. A., Ducci, M., Stevenson, D. J., Lunine, J. I., Armstrong, J. W., … Tortora, P. (2012). The tides of Titan. *Science*, *337*(6093), 457–459. https://doi.org/10.1126/science.1219631

Iess, L., Stevenson, D. J., Parisi, M., Hemingway, D., Jacobson, R. A., Lunine, J. I., … Tortora, P. (2014). The gravity field and interior structure of Enceladus. *Science*, *344*(6179), 78–80. https://doi.org/10.1126/science.1250551

Isaak, D. G., & Masuda, K. (1995). Elastic and viscoelastic properties of α iron at high temperatures. *Journal of Geophysical Research*, *100*(B9), 17,689–17,698. https://doi.org/10.1029/95JB01235

Jacobson, R. A., Antreasian, P. G., Bordi, J. J., Criddle, K. E., Ionasescu, R., Jones, J. B., … Stauch, J. R. (2006). The gravity field of the saturnian system from satellite observations and spacecraft tracking data. *The Astronomical Journal*, *132*(6), 2520–2526. https://doi.org/10.1086/508812

Journaux, B., Daniel, I., Caracas, R., Montagnac, G., & Cardon, H. (2013). Influence of NaCl on ice VI and ice VII melting curves up to 6 GPa, implications for large icy moons. *Icarus*, *226*(1), 355–363. https://doi.org/10.1016/j.icarus.2013.05.039

Journaux, B., Daniel, I., Petitgirard, S., Cardon, H., Perrillat, J.-P., Caracas, R., & Mezouar, M. (2017). Salt partitioning between water and high-pressure ices. Implication for the dynamics and habitability of icy moons and water-rich planetary bodies. *Earth and Planetary Science Letters*, *463*, 36–47. https://doi.org/10.1016/j.epsl.2017.01.017

Kalousová, K., Sotin, C., Choblet, G., Tobie, G., & Grasset, O. (2018). Two-phase convection in Ganymede's high-pressure ice layer—Implications for its geological evolution. *Icarus*, *299*, 133–147. https://doi.org/10.1016/j.icarus.2017.07.018

Kamata, S., Matsuyama, I., & Nimmo, F. (2015). Tidal resonance in icy satellites with subsurface oceans. *Journal of Geophysical Research: Planets*, *120*, 1528–1542. https://doi.org/10.1002/2015JE004821

Kamata, S., Kimura, J., Matsumoto, K., Nimmo, F., Kuramoto, K., & Namiki, N. (2016). Tidal deformation of Ganymede: Sensitivity of Love numbers on the interior structure. *Journal of Geophysical Research: Planets*, *121*, 1362–1375. https://doi.org/10.1002/2016JE005071

Karato, S. (1990). The role of hydrogen in the electrical conductivity of the upper mantle. *Nature*, *347*(6290), 272–273. https://doi.org/10.1038/347272a0

Kern, H. (1990). Laboratory seismic measurements: An aid in the interpretation of seismic field data. *Terra Nova*, *2*(6), 617–628. https://doi.org/10.1111/j.1365-3121.1990.tb00127.x

Kite, E. S., & Rubin, A. M. (2016). Sustained eruptions on Enceladus explained by turbulent dissipation in tiger stripes. *Proceedings of the National Academy of Sciences*, *113*(15), 3972–3975. https://doi.org/10.1073/pnas.1520507113

Kivelson, M., Khurana, K., & Volwerk, M. (2002). The permanent and inductive magnetic moments of Ganymede. *Icarus*, *157*(2), 507–522. https://doi.org/10.1006/icar.2002.6834

Klotz, S., & Braden, M. (2000). Phonon dispersion of bcc iron to 10 GPa. *Physical Review Letters*, *85*(15), 3209–3212. https://doi.org/10.1103/physrevlett.85.3209

Kozlovsky, Y. A. (1987). Geothermic investigations. *Exploration of the Deep Continental Crust* (pp. 387–393). Berlin: Springer. https://doi.org/10.1007/978-3-642-71137-4_24

Larionov, E. G., & Kryukov, P. A. (1984). The conductivity of MgSO4 aqueous-solutions in the range of temperatures 298-423K and pressures 0,1-784,6 MPa. *Izvestiya Sibirskogo Otdeleniya Akademii Nauk SSSR Seriya Khimicheskikh Nauk*, *5*, 20–23.

Lefevre, A., Tobie, G., Choblet, G., & Čadek, O. (2014). Structure and dynamics of titan's outer icy shell constrained from Cassini data. *Icarus*, *237*, 16–28. https://doi.org/10.1016/j.icarus.2014.04.006

Lemmon, E. W., Huber, M. L., & McLinden, M. O. (2007). NIST reference fluid thermodynamic and transport properties-REFPROP. Boulder, CO: Physical and Chemical Properties Division, National Institute of Standards and Technology.

Mantegazzi, D., Sanchez-Valle, C., & Driesner, T. (2013). Thermodynamic properties of aqueous NaCl solutions to 1073K and 4.5GPa, and implications for dehydration reactions in subducting slabs. *Geochimica et Cosmochimica Acta*, *121*, 263–290. https://doi.org/10.1016/j.gca.2013.07.015

Marshall, W. L. (1987). Reduced state relationship for limiting electrical conductances of aqueous ions over wide ranges of temperature and pressure. *The Journal of Chemical Physics*, *87*(6), 3639–3643. https://doi.org/10.1063/1.452960

Masters, G., Laske, G., Bolton, H., & Dziewonski, A. (2000). The relative behavior of shear velocity, bulk sound speed, and compressional velocity in the mantle: Implications for chemical and thermal structure, *Earth's deep interior: Mineral physics and tomography from the atomic to the global scale, Geophysical Monograph Series* (Vol. 117, pp. 63–87). Washington, DC: American Geophysical Union. https://doi.org/10.1029/gm117p0063

Mazarico, E., Genova, A., Neumann, G. A., Smith, D. E., & Zuber, M. T. (2015). Simulated recovery of Europa's global shape and tidal Love numbers from altimetry and radio tracking during a dedicated flyby tour. *Geophysical Research Letters*, *42*, 3166–3173. https://doi.org/10.1002/2015GL063224

McDougall, T. J., & Barker, P. M. (2011). Getting started with TEOS-10 and the Gibbs Seawater (GSW) oceanographic toolbox. *SCOR/IAPSO WG*, *127*, 1–28.

McKinnon, W. B. (2006). On convection in ice I shells of outer Solar System bodies, with detailed application to Callisto. *Icarus*, *183*(2), 435–450. https://doi.org/10.1016/j.icarus.2006.03.004

McKinnon, W. B. (2015). Effect of Enceladus's rapid synchronous spin on interpretation of Cassini gravity. *Geophysical Research Letters*, *42*, 2137–2143. https://doi.org/10.1002/2015GL063384

Millero, F. J., Feistel, R., Wright, D. G., & McDougall, T. J. (2008). The composition of standard seawater and the definition of the reference-composition salinity scale. *Deep Sea Research Part I: Oceanographic Research Papers*, *55*(1), 50–72. https://doi.org/10.1016/j.dsr.2007.10.001

Mitri, G., Meriggiola, R., Hayes, A., Lefevre, A., Tobie, G., Genova, A., … Zebker, H. (2014). Shape, topography, gravity anomalies and tidal deformation of Titan. *Icarus*, *236*, 169–177. https://doi.org/10.1016/j.icarus.2014.03.018

Moore, W. B., & Schubert, G. (2003). The tidal response of Ganymede and Callisto with and without liquid water oceans. *Icarus*, *166*(1), 223–226. https://doi.org/10.1016/j.icarus.2003.07.001

Müntener, O. (2010). Serpentine and serpentinization: A link between planet formation and life. *Geology*, *38*(10), 959–960. https://doi.org/10.1130/focus102010.1

Panning, M. P., Stähler, S. C., Huang, H.-H., Vance, S. D., Kedar, S., Tsai, V. C., … Lorenz, R. D. (2018). Expected seismicity and the seismic noise environment of Europa. *Journal of Geophysical Research*, *123*, 163–179. https://doi.org/10.1002/2017JE005332

Pappalardo, R., Prockter, L., Senske, D., Klima, R., Fenton Vance, S., & Craft, K. (2016). Science objectives and capabilities of the NASA Europa Mission. In *47th Lunar and Planetary Science Conference*, Texas (pp. 3058).

Park, R. S., Bills, B., Buffington, B. B., Folkner, W. M., Konopliv, A. S., Martin-Mur, T. J., … Watkins, M. M. (2015). Improved detection of tides at Europa with radiometric and optical tracking during flybys. *Planetary and Space Science*, *112*, 10–14. https://doi.org/10.1016/j.pss.2015.04.005

Peacock, S. M., Christensen, N. I., Bostock, M. G., & Audet, P. (2011). High pore pressures and porosity at 35 km depth in the Cascadia subduction zone. *Geology*, *39*(5), 471–474. https://doi.org/10.1130/g31649.1

Postberg, F., Schmidt, J., Hillier, J., Kempf, S., & Srama, R. (2011). A salt-water reservoir as the source of a compositionally stratified plume on Enceladus. *Nature*, *474*(7353), 620–622. https://doi.org/10.1038/nature10175

Saito, M. (1974). Some problems of static deformation of the Earth. *Journal of Physics of the Earth*, *22*(1), 123–140. https://doi.org/10.4294/jpe1952.22.123

Saito, S., Ishikawa, M., Arima, M., & Tatsumi, Y. (2016). Laboratory measurements of V_p and V_s in a porosity-developed crustal rock: Experimental investigation into the effects of porosity at deep crustal pressures. *Tectonophysics*, *677–678*, 218–226. https://doi.org/10.1016/j.tecto.2016.03.044

Sanloup, C., Guyot, F., Gillet, P., Fiquet, G., Mezouar, M., & Martinez, I. (2000). Density measurements of liquid Fe-S alloys at high-pressure. *Geophysical Research Letters*, *27*(6), 811–814. https://doi.org/10.1029/1999GL008431

Schmidt, C., & Manning, C. (2017). Pressure-induced ion pairing in $MgSO_4$ solutions: Implications for the oceans of icy worlds. *Geochemical Perspectives Letters*, *3*, 66–74.

Schubert, G., Anderson, J., Spohn, T., & McKinnon, W. (2004). Interior composition, structure and dynamics of the Galilean satellites. In F. Bagenal, T. E. Dowling, & W. B. McKinnon (Eds.), *Jupiter. The planet, satellites and magnetosphere* (Vol. 1, pp. 281–306), Cambridge planetary science. Cambridge, UK: Cambridge University Press.

Shaw, G. H. (1986). Elastic properties and equation of state of high pressure ice. *The Journal of Chemical Physics*, *84*(10), 5862–5868. https://doi.org/10.1063/1.449897

Shock, E. L., & Holland, M. E. (2007). Quantitative habitability. *Astrobiology*, *7*(6), 839–851. https://doi.org/10.1089/ast.2007.0137

Sohl, F., Choukroun, M., Kargel, J., Kimura, J., Pappalardo, R., Vance, S., & Zolotov, M. (2010). Subsurface water oceans on icy satellites: Chemical composition and exchange processes. *Space Science Reviews*, *153*(1–4), 485–510. https://doi.org/10.1007/s11214-010-9646-y

Stähler, S. C., Panning, M. P., Vance, S. D., vanDriel, M., Nissen-Meyer, T., Lorenz, R. D., & Kedar, S. (2018). Seismic wave propagation in icy ocean worlds. *Journal of Geophysical Research: Planets*, *123*, 206–232. https://doi.org/10.1002/2017JE005338

Steinbrügge, G., Stark, A., Hussmann, H., Sohl, F., & Oberst, J. (2015). Measuring tidal deformations by laser altimetry. A performance model for the Ganymede Laser Altimeter. *Planetary and Space Science*, *117*, 184–191. https://doi.org/10.1016/j.pss.2015.06.013

Stixrude, L., & Lithgow-Bertelloni, C. (2011). Thermodynamics of mantle minerals. II. Phase equilibria. *Geophysical Journal International*, *184*(3), 1180–1213. https://doi.org/10.1111/j.1365-246X.2010.04890.x

Takeuchi, H., Saito, M., & Bolt, B. (1972). Seismic surface waves. *Methods in Computational Physics*, *11*, 217–295.

Thomas, P. (2010). Sizes, shapes, and derived properties of the Saturnian satellites after the Cassini nominal mission. *Icarus*, *208*(1), 395–401. https://doi.org/10.1016/j.icarus.2010.01.025

Thomas, P., Tajeddine, R., Tiscareno, M., Burns, J., Joseph, J., Loredo, T., … Porco, C. (2016). Enceladus's measured physical libration requires a global subsurface ocean. *Icarus*, *264*, 37–47. https://doi.org/10.1016/j.icarus.2015.08.037

Tillner-Roth, R., & Friend, D. G. (1998). A helmholtz free energy formulation of the thermodynamic properties of the mixture {Water + Ammonia}. *Journal of Physical and Chemical Reference Data*, *27*(1), 63–96. https://doi.org/10.1063/1.556015

Tobie, G., Mocquet, A., & Sotin, C. (2005). Tidal dissipation within large icy satellites: Applications to Europa and Titan. *Icarus*, *177*(2), 534–549. https://doi.org/10.1016/j.icarus.2005.04.006

Todd, T., & Simmons, G. (1972). Effect of pore pressure on the velocity of compressional waves in low-porosity rocks. *Journal of Geophysical Research*, *77*(20), 3731–3743. https://doi.org/10.1029/JB077i020p03731

Tutolo, B. M., Mildner, D. F., Gagnon, C. V., Saar, M. O., & Seyfried, W. E. (2016). Nanoscale constraints on porosity generation and fluid flow during serpentinization. *Geology*, *44*(2), 103–106. https://doi.org/10.1130/g37349.1

Ulmer, P., & Trommsdorff, V. (1995). Serpentine stability to mantle depths and subduction-related magmatism. *Science*, *268*(5212), 858–861. https://doi.org/10.1126/science.268.5212.858

Van Hoolst, T., Baland, R.-M., & Trinh, A. (2013). On the librations and tides of large icy satellites. *Icarus*, *226*(1), 299–315. https://doi.org/10.1016/j.icarus.2013.05.036

Vance, S. (2017). vancesteven/planetprofile: Release for use in reproducing results submitted to Journal of Geophysical Research: Planets, Zenodo. https://doi.org/10.5281/zenodo.844131

Vance, S., & Brown, J. M. (2013). Thermodynamic properties of aqueous $MgSO_4$ to 800 MPa at temperatures from −20 to 100°C and concentrations to 2.5 mol kg^{-1} from sound speeds, with applications to icy world oceans. *Geochimica et Cosmochimica Acta*, *110*, 176–189. https://doi.org/10.1016/j.gca.2013.01.040

Vance, S., Harnmeijer, J., Kimura, J., Hussmann, H., deMartin, B., & Brown, J. M. (2007). Hydrothermal systems in small ocean planets. *Astrobiology*, *7*(6), 987–1005. https://doi.org/10.1089/ast.2007.0075

Vance, S., Bouffard, M., Choukroun, M., & Sotin, C. (2014). Ganymede's internal structure including thermodynamics of magnesium sulfate oceans in contact with ice. *Planetary and Space Science*, *96*, 62–70. https://doi.org/10.1016/j.pss.2014.03.011

Vance, S. D., Hand, K. P., & Pappalardo, R. T. (2016). Geophysical controls of chemical disequilibria in Europa. *Geophysical Research Letters*, *43*, 4871–4879. https://doi.org/10.1002/2016GL068547

Vance, S., Tsai, V., Kedar, S., Bills, B., Castillo-Rogez, J., & Jackson, J. (2016). Seismic investigations of Europa and other ocean worlds. *EGU General Assembly 2016, held 17-22 April, 2016 in Vienna Austria, id. EPSC2016-5372*.

Vance, S., Tsai, V., Kedar, S., Bills, B., Castillo-Rogez, J., & Jackson, J. (2017). Vital signs: Seismology of ocean worlds. *Astrobiology, in press, arXiv preprint arXiv:1610.10,067*.

Vitovtova, V. M., Shmonov, V. M., & Zharikov, A. V. (2014). The porosity trend and pore sizes of the rocks in the continental crust of the Earth: Evidence from experimental data on permeability. *Izvestiya. Physics of the Solid Earth*, *50*(5), 593–602. https://doi.org/10.1134/s1069351314040181

Vogt, C., Laihem, K., & Wiebusch, C. (2008). Speed of sound in bubble-free ice. *The Journal of the Acoustical Society of America*, *124*(6), 3613–3618. https://doi.org/10.1121/1.2996304

Voronov, F. F., & Chernysheva, E. V. (1999). Anomalies in the elastic properties of silicious iron single crystals at pressures of up to 9 GPa and the $\alpha - \epsilon$ phase transformation. *Physics of the Solid State*, *41*(3), 462–467. https://doi.org/10.1134/1.1130804

Wahr, J., Selvans, Z. A., Mullena, M. E., Barr, A. C., Collins, G. C., Selvans, M. M., … Pappalardo, R. T. (2009). Modeling stresses on satellites due to nonsynchronous rotation and orbital eccentricity using gravitational potential theory. *Icarus*, *200*, 188–206. https://doi.org/10.1016/j.icarus.2008.11.002

Waite, J. H., Glein, C. R., Perryman, R. S., Teolis, B. D., Magee, B. A., Miller, G., … Scott J. Bolton (2017). Cassini finds molecular hydrogen in the Enceladus plume: Evidence for hydrothermal processes. *Science*, *356*(6334), 155–159. https://doi.org/10.1126/science.aai8703

Wang, D., Mookherjee, M., Xu, Y., & Karato, S.-I. (2006). The effect of water on the electrical conductivity of olivine. *Nature*, *443*(7114), 977–980. https://doi.org/10.1038/nature05256

Wang, X.-Q., Schubnel, A., Fortin, J., David, E. C., Guéguen, Y., & Ge, H.-K. (2012). High Vp/Vs ratio: Saturated cracks or anisotropy effects? *Geophysical Research Letters*, *39*, L11307. https://doi.org/10.1029/2012GL051742

Wyllie, M. R. J., Gregory, A. R., & Gardner, G. H. F. (1958). An experimental investigation of factors affecting elastic wave velocities in porous media. *Geophysics*, *23*(3), 459–493. https://doi.org/10.1190/1.1438493

Xu, Y., Shankland, T. J., & Poe, B. T. (2000). Laboratory-based electrical conductivity in the Earth's mantle. *Journal of Geophysical Research*, *105*(B12), 27,865–27,875. https://doi.org/10.1029/2000JB900299

Yoshino, T., Matsuzaki, T., Shatskiy, A., & Katsura, T. (2009). The effect of water on the electrical conductivity of olivine aggregates and its implications for the electrical structure of the upper mantle. *Earth and Planetary Science Letters*, *288*(1–2), 291–300. https://doi.org/10.1016/j.epsl.2009.09.032

Yu, C., Ji, S., & Li, Q. (2016). Effects of porosity on seismic velocities, elastic moduli and Poisson's ratios of solid materials and rocks. *Journal of Rock Mechanics and Geotechnical Engineering*, *8*(1), 35–49. https://doi.org/10.1016/j.jrmge.2015.07.004

Zhao, C., & Yoshino, T. (2016). Electrical conductivity of mantle clinopyroxene as a function of water content and its implication on electrical structure of uppermost mantle. *Earth and Planetary Science Letters*, *447*, 1–9. https://doi.org/10.1016/j.epsl.2016.04.028

Zolotov, M. (2008). Oceanic composition on Europa: Constraints from mineral solubilities. In *39th Lunar and Planetary Science Conference, (Lunar and Planetary Science XXXIX)*, 2349, League City, Texas.

Zolotov, M. Y., & Kargel, J. (2009). On the chemical composition of Europa's icy shell, ocean, and underlying rocks. In R. T. Pappalardo, W. B. McKinnon, & K. Khurana (Eds.), *Europa* (pp. 431–458). Tucson, AZ: University of Arizona Press.

Erratum

Table 9 as originally published contained errors. A logical error in the code led to a miscalculation of iceV thicknesses for Jupiter's moon Callisto. An incorrect value for the internal heat, Q_{rock} (110 GW instead of 130 GW) was also listed. The schematic of Callisto in Figure 4 is correct. Table 9 has been corrected, and the current version may be considered the version of record.